

Summer Season Precipitation Biases in 4 km WRF Forecasts Over Southern China: Diagnoses of the Causes of Biases

Kefeng Zhu¹ , Biyu Yu^{2,3}, Ming Xue^{2,4} , Bowen Zhou² , and Xiao-Ming Hu⁴

¹Nanjing Joint Institute for Atmospheric Sciences and CMA Key Laboratory of Transportation Meteorology, Nanjing, China, ²Key Laboratory of Mesoscale Severe Weather/Ministry of Education and School of Atmospheric Sciences, Nanjing University, Nanjing, China, ³East China Regional Air Traffic Management Bureau of Civil Aviation of China, Shanghai, China, ⁴Center for Analysis and Prediction of Storms and School of Meteorology, University of Oklahoma, Norman, Ok, USA

Key Points:

- The initiation and propagation of convection over southern China are greatly influenced by land-sea circulations
- Cold bias over land results in a weaker sea breeze during the afternoon and a stronger land breeze at night, causing rainfall location bias
- Overprediction of moisture along the coastal mountains and over the ocean is the primary cause of excessive rainfall

Correspondence to

M. Xue,
mxue@ou.edu

Citation:

Zhu, K., Yu, B., Xue, M., Zhou, B., & Hu, X.-M. (2021). Summer season precipitation biases in 4 km WRF forecasts over southern China: Diagnoses of the causes of biases. *Journal of Geophysical Research: Atmospheres*, 126, e2021JD035530. <https://doi.org/10.1029/2021JD035530>

Received 6 JUL 2021
Accepted 18 NOV 2021

Author Contributions:

Data curation: Kefeng Zhu, Biyu Yu
Formal analysis: Kefeng Zhu
Methodology: Kefeng Zhu
Software: Biyu Yu
Supervision: Ming Xue
Writing – original draft: Kefeng Zhu
Writing – review & editing: Ming Xue, Bowen Zhou, Xiao-Ming Hu

Abstract In a recent study, we evaluated the performance of real-time convection-permitting WRF model forecasting over China. Although the overall rainfall distribution and diurnal cycle are well simulated, the model greatly overestimates the rainfall intensity in southern China and the predicted rainfall shows a southeast location bias. In this study, possible factors contributing to the precipitation forecast bias are discussed. The precipitation over southern China is found to be greatly influenced by land-sea circulations. While the model captures diurnal variations of winds well, the predicted amplitude and onset timing of the land/sea breezes differ from observations. Cold bias of land-surface temperature is shown to partially cause wind bias. In the afternoon, the cold bias results in a weakened inland penetration of sea breeze, which in turn leads to more rain on the eastern south-China coastline. During nighttime, excessive cooling over land results in a stronger land breeze, leading to location bias of early morning precipitation. While the observed coastal rain belt is mostly located over land during early morning, the predicted coastal rain belt is mostly located over ocean. In addition, the model overestimates moisture at low levels, especially over the southern slope of the coastal mountains and over ocean, which explains the excessive rainfall over southern China. This study emphasizes the importance of accurately simulating land-surface-related variables for precipitation forecast in coastal regions where land-sea contrast plays an important role.

1. Introduction

Summer (June–August) rainfall accounts for 50%–80% of the total annual rainfall for most regions in China (Dong et al., 2016; Zhu et al., 2018b). There are three major summer precipitation centers in China (Ding, 1992; Zhu et al., 2018a). One is along the Yangtze-Huaihe River Valley, where the precipitation is mainly due to the Meiyu front (Tao, 1980; Sun & Zhang 2012; Jin et al., 2013; Xue et al., 2018). One is in the Sichuan Basin that is known for the ‘Bashan Yeyu’ (nocturnal precipitation in the Bashan Mountains) (Lv 1942; Chen et al., 2010; Jin et al., 2013; Zhang et al., 2019). The other region is in southern China (mainly in Guangdong Province) (Chen et al., 2014; Luo et al., 2017), which has the richest warm and moist air supply in China. Among the three precipitation centers, southern China has the heaviest rainfall (Luo et al., 2013; Zheng et al., 2016) in terms of both frequency and intensity (Zhang et al., 2017; Bai et al., 2020a).

Southern China is characterized by abundant atmospheric water vapor, common occurrence of thermodynamic instabilities, and external forcing due to its complex topography (Figure 1) and land-sea thermal contrast, which often collectively result in abrupt and intense moist convection (He et al., 2016). There are many mesoscale processes that could cause heavy rainfall, including cold fronts or quasi-stationary fronts (Huang et al., 1986), wind shear lines (Wang et al., 2014), synoptic and boundary-layer low-level jets (Du & Chen 2018), mesoscale vortices (Chang et al., 1998), and gravity waves (Du & Rotunno 2018). Complex land-surface properties, such as multiscale terrain and large urban agglomerations, can further complicate the heavy rainfall formation and development. Rainfall maxima are often found on the windward side of mountains (Xu et al., 2009; Li et al., 2020a). Urbanization likely increases the frequency of extreme rainfall in urban areas (Wu et al., 2019; Yan et al., 2020; Yin et al., 2020). In recent decades, great efforts have been made to understand the characteristics and mechanisms of heavy rainfall in southern China (Luo et al., 2013; Wang et al., 2014; Bai et al., 2020b). Some of the progresses are summarized in review papers by Lu (2019), Sun et al. (2019), and Luo et al. (2020).

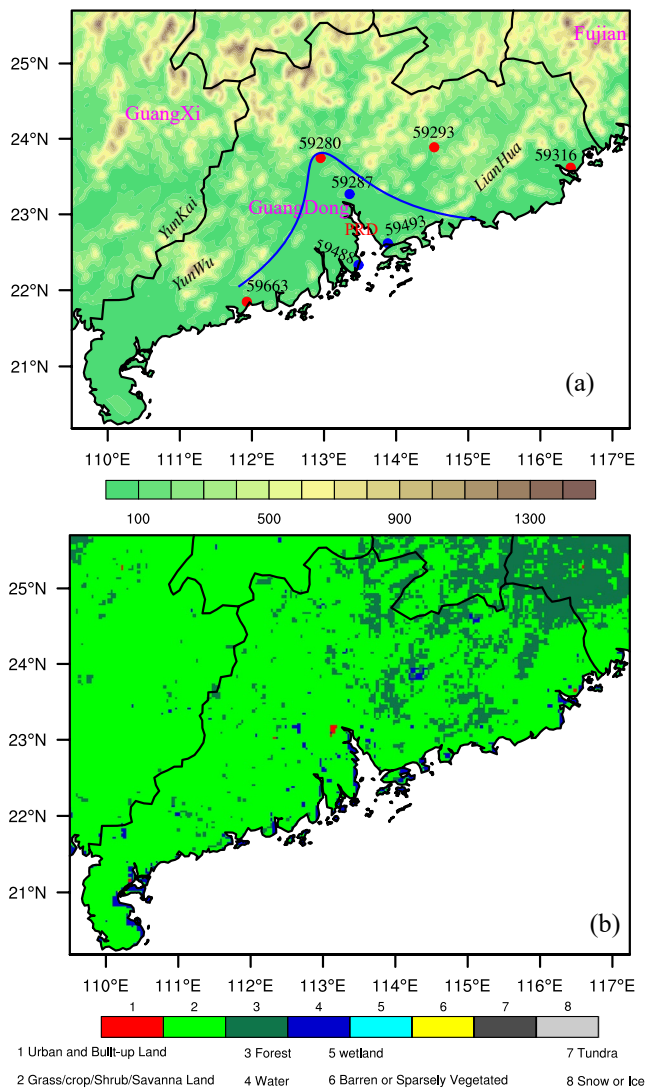


Figure 1. (a) The verification domain of Southern China. Terrain height is shown in gray shaded contours at 500-m intervals. The red dots mark the four sounding sites in Guangdong Province and the blue dots are the selected national standard level surface stations along the coastline of the Pearl River Delta (PRD) region. Mountains within Guangdong Province are marked in Italic. (b) The land type category from the USGS datasets. The blue line denotes the approximate boundary between mountain and plain.

Precipitation diurnal variation over southern China shows two clear peaks: an afternoon peak and an early morning peak. Apart from the narrow strip of rainfall that occurs along the southern coastline during the early morning peak, the afternoon peak dominates the inland region (Li et al., 2008; Zhu et al., 2018a). Chen et al. (2016) used three years of radar observations to study the precipitation diurnal cycle over the Pearl River Delta (PRD) in southern China. They found that the precipitation diurnal variation during the early summer is closely related to the land-sea circulations. The nocturnal peak is related to the convergence line at the leading edge of the enhanced low-level jet and the land breeze during the night (Du & Chen 2019; Liu et al., 2020), whereas the afternoon peak is related to local convection initiation due to intense solar surface heating (Romatschke & Houze 2011; Chen et al., 2014) and convection propagation associated with the sea breeze (Jiang et al., 2017). During the summer period, warm and moist air with high convective instability within the prevailing monsoon flows provide favorable conditions for convection initiation. The sea (land) breeze combined with valley (mountain) breeze induced by coastal terrain further enhances onshore (offshore) winds. These near-surface flows have substantial impact on water vapor transport and flow convergence at low levels, which in turn affects the initiation and evolution of convection over southern China (Zheng et al., 2013).

Despite the progresses in understanding the rainfall characteristics and mechanisms of heavy rainfall over southern China, there are relatively few studies on the performance of convection-permitting model over the region over sufficiently long periods. Previous precipitation studies in the region are mostly based on case studies with focus on specific types of heavy rainfall. Zhang and Meng (2019) evaluated model performance of 45 warm-sector heavy rain cases prediction over southern China. Three two-way nested domains and 27, 9, and 3 horizontal grid spacings were used. They found that the overprediction of the northward low-level jet (below 900 hPa) intensity leads to underestimation of convection along the southern coastline, resulting in a lower quantitative precipitation forecast skill. Wu et al. (2020) investigated the predictability of a warm-sector heavy rainfall event using convection-permitting ensemble forecasts. Their results show that good ensemble members simulate stronger low-level southerly winds over the sea and more accurate land/mountain breezes than bad members. The forecast bias of low-level winds and the regional circulations induced by the bias in local thermal contrast are suggested as possible error sources of the precipitation forecast. Furtado et al. (2018) and Furtado et al. (2020) investigated the effects of cloud microphysics scheme and cloud-aerosol interactions on South China heavy rainfall events, and showed strong sensitivity to the choice of microphysics scheme, and to the indirect effects of aerosols.

Compared with mesoscale convective systems associated with, e.g., cold/stationary fronts and mesoscale vortices, the frequent moist convection over southern China is much harder to predict and the error sources of position and intensity biases are not well understood (Chang et al., 2017). In a recent study, we evaluated the performance of convection-permitting forecasts with the Weather Research and Forecast (WRF) model over China in two summer seasons (Zhu et al., 2018a). Overall, the 4 km WRF precipitation forecasts showed good agreement with observations for most parts of China, outperforming global model forecasts from major NWP centers in terms of the spatial distribution and diurnal variations of rainfall. However, the location of rainfall systems over southern China were not predicted well (Yu et al., 2020), and the rainfall intensity along the coastline is clearly overpredicted. As pointed out earlier, southern China has abundant moisture and instability, and convection is often generated under weak synoptic conditions (Luo et al., 2016). The low-level conditions and land-surface properties may have a profound impact on the formation and evolution of rainfall systems in the region. This study aims to

identify the primary cause of the precipitation biases mentioned above, with emphasis on correlations between precipitation forecast bias and forecast bias in low-level thermodynamic variables, winds, and land-sea thermal contrast, as well as cause-and-effect relationship.

The rest of paper is organized as follows. The forecast data and observations used in this study are briefly introduced. A general evaluation of the 4 km WRF model performance, together with an overview of the land-sea circulations over the study domain and their relationship with precipitation formation and propagation, are given in Section 3. In Section 4, we focus on factors that have substantial impact on the landsea circulations, and their relationship with precipitation forecast biases. A summary and future work are given in Section 5.

2. Forecast Model Configuration and Observations

The forecast data used in this study are from the real-time WRF forecasts run at Nanjing University, China every summer since 2013 (Zhu et al., 2018a). The horizontal grid-spacing is 4 km (4 km WRF hereafter) and the model has 51 vertical levels. The midpoint of the first layer is about 13 m above ground, and the layer depth is about 26 m. There are roughly 10 levels in the lowest 1 km. The 4 km WRF covers the entire mainland China. The initial and lateral boundary conditions, including sea-surface temperature, are from the NCEP Global Forecast System (GFS) real-time analysis and forecasts, respectively (0.5° grid spacing before 27 June 2016 and 0.25° afterwards). Key physics parameterizations include the Morrison double-moment microphysics scheme (Morrison et al., 2005), the Asymmetrical Convective Model version 2 (ACM2) planetary boundary layer (PBL) scheme (Pleim, 2007), the Pleim-Xiu (PLX) land surface and surface layer schemes (Pleim & Xiu 1995), and the CAM radiation scheme (Collins et al., 2004). More details on the configurations can be found in Zhu et al. (2018a).

The model topography uses the 30s Global Multi-resolution Terrain Elevation Data 2010. A clear \wedge -shaped mountain range is seen in southern China (see blue line in Figure 1a). The land cover data use the 30s U.S. Geological Survey (USGS) data set 2010, which significantly underestimates the urban area over the region of PRD (see Figure 1b). Cheng et al. (2013) show a similar issue for the USGS data set over Taiwan. As we will discuss later in Section 4b, this is an important reason for the temperature underestimation over the PRD urban region.

This study focuses on precipitation over southern China, mostly in Guangdong Province (see Figure 1a) during summer (June-August) 2016. The 12-36 h forecasts initiated every day at 1200 UTC are examined, which are beyond the precipitation spin up period. Seventeen days during the period that were influenced by typhoon are excluded because such strongly forced days tend to have different precipitation bias behaviors. As mentioned above, high instability with abundant moisture together with orographic thermal and dynamic forcing over southern China provide favorable conditions for convection formation, even under weak synoptic conditions. Special attention will be paid to the accuracy of forecast variables at the low levels, including wind, temperature, and moisture.

Observations and derived products at low levels over southern China have been collected, including surface station observations, gridded hourly precipitation and 2 m temperature, and the National Centers for Environmental Prediction (NCEP) final analysis (FNL). The hourly precipitation is a $0.05^\circ \times 0.05^\circ$ merged precipitation analysis product (over 70° – 140° E, 15° – 60° N) produced by the China Meteorological Administration (CMA) (Shen et al., 2014; Pan et al., 2015), based on the corrected Climate Prediction Center's morphing rainfall estimates (CMORPH) data set (Joyce et al., 2004) and over 30,000 rain-gauge observations. Previous verification against independent observations indicates that this data set is reliable over southern China (Luo et al., 2013) and other regions (Wu et al., 2018; Li et al., 2020b; Zhao et al., 2020; Li et al., 2021). In a recent paper, we also used this gridded data set to perform multi-scale evaluation of the performance of 4 km and 12 km WRF model forecasts over China (Yu et al., 2020).

The hourly gridded 2 m temperature is from the CMA land-surface data assimilation system (CLDAS) (Shi et al., 2011). It has a grid resolution of $0.0625^\circ \times 0.0625^\circ$ and covers 60° – 160° E, 0° – 65° N. Verification against 2400 national surface stations (from the website: http://data.cma.cn/data/detail/dataCode/NAFP_CLDAS2.0_NRT.html) shows that the mean bias of the CLDAS 2 m temperature data set is -0.13 K and the root mean square error is 0.88 K. The correlation of the analysis and observations is as high as 0.97. The NCEP $0.25^\circ \times 0.25^\circ$ FNL 6-hourly analyses are used to evaluate moisture fields at low levels. The FNL analyses are made with the same operational GFS data assimilation system but are rerun with time delay for more observations to arrive. We have calculated the mean biases of the water vapor mixing ratio in the real-time analysis relative to the FNL

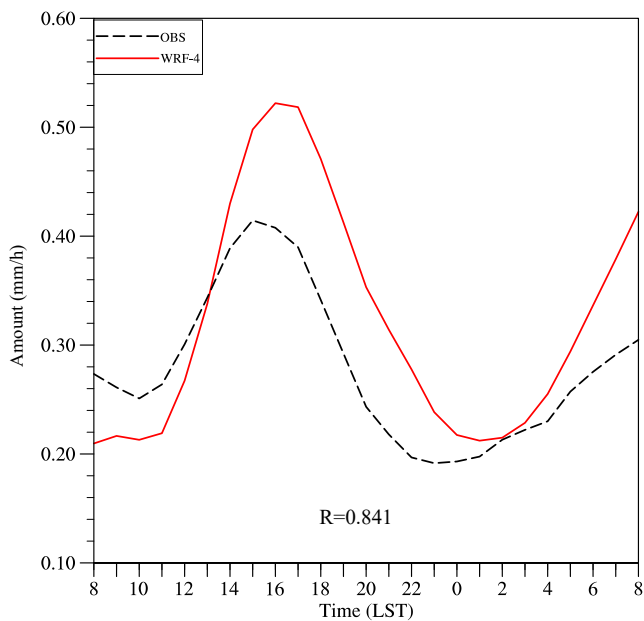


Figure 2. Times series of observed (OBS) and simulated (WRF) temporally and spatially (with the domain of Figure 1) averaged hourly rainfall over southern China during summer 2016. Here, 17 days influenced by typhoon are excluded. The same for the rest of figures.

for the three investigated model levels. The differences between FNL and the real-time analysis are very small. The mean biases are $-2.4 \times 10^{-5} \text{ g kg}^{-1}$, $3.7 \times 10^{-4} \text{ g kg}^{-1}$, $-5.4 \times 10^{-4} \text{ g kg}^{-1}$ for the surface, 925 hPa and 850 hPa levels, respectively. The FNL analyses are regularly used to verify GFS forecasts. Since we use GFS analysis as the initial condition for the WRF forecast, we choose to use FNL analyses to verify the WRF forecasts.

Other verification data used in this study include soundings at four sites (red dots in Figure 1a) and hourly surface observations at three surface stations (blue dots in Figure 1a) along the coastline of the PRD region. The sounding observations are usually conducted twice a day at 0000 UTC (0800 LST) and 1200 UTC (2000 LST). Two sites, No. 52980 and 59316, have additional 0600 UTC (1400 LST) sounding launches during the rainy season.

3. Precipitation Over Southern China and Its Relationship With Land-Sea Circulations

3.1. Evaluation of 4 km WRF Precipitation Forecasts Over Southern China

Precipitation diurnal variation over southern China has two peaks: one at 1500 LST and the other at 0800 LST (Figure 2). The afternoon peak is larger than the morning peak, consistent with previous findings of high-frequency afternoon convection contributing most of the rainfall in the region (Jiang et al., 2017). Afternoon convection is most often triggered as a result of solar heating (Luo et al., 2013; Chen et al., 2015). The WRF forecasts successfully reproduce the twin-peak pattern but overpredict the magnitude of both peaks.

The time series correlation between observations and forecasts is as high as 0.84. However, timing of the predicted afternoon peak is delayed by about one hour.

During the afternoon in summer 2016, there are three main precipitation belts in the season mean observed precipitation field (Figure 3a): one is over the western part of Guangdong Province (hereafter, WG), mostly over the Yunkai Mountains and on the south sides of the coastal Yunwu Mountains; the second is over the eastern part of Guangdong Province (hereafter, EG), mostly on the south side of coastal Lianhua Mountains; and the third one is in the middle of Guangdong Province (hereafter, MG), mainly on the upstream side of the ^-shaped mountains (black contours represent terrain height). In general, afternoon precipitation on the windward side of the coastal mountains is found to be greatly influenced by the sea breeze and the upslope winds (Zheng et al., 2013; Jiang et al., 2017), whereas precipitation over the mountains is mostly triggered by surface heating (Chen et al., 2015). The WRF forecasts successfully reproduce the rain belts over mountains and on the southern slope of the coastal mountains of WG and EG (Figure 3b). However, compared to the observations, the forecasts produce much higher precipitation amount over both EG and WG, especially the former. As discussed in the next section, this is probably due to the systematic eastward direction bias of the surface winds. For MG, the forecast fails to reproduce the location of the rainfall maximum near the center of the subregion. The predicted rainfall is mostly located near the coast whereas the observed maximum is about a hundred kilometers inland, on the south side of mountains and also over the most urbanized region. There is also too much precipitation at the border of MG and EG regions.

During the early morning, the observed precipitation is mostly along the coastline (Figure 3c). This is consistent with a previous study that shows the precipitation likely forms along the convergence line between land breeze and enhanced southerly nocturnal low-level jet (Chen et al., 2016). Similar to the rainfall during afternoon, the forecasts show excessive rainfall amount over EG. There is also major difference with the rain belt along the coastline. The predicted rain belt is mostly located off the coast over ocean (Figure 3d), whereas the observed rain belt is mostly along the coastline (Figure 3c). For both afternoon and early morning periods, the rainfall intensity is overpredicted. The average amount of predicted precipitation center is mostly over 5 mm h^{-1} (between red and purple colors) whereas the observed precipitation amount is generally under 5 mm h^{-1} .

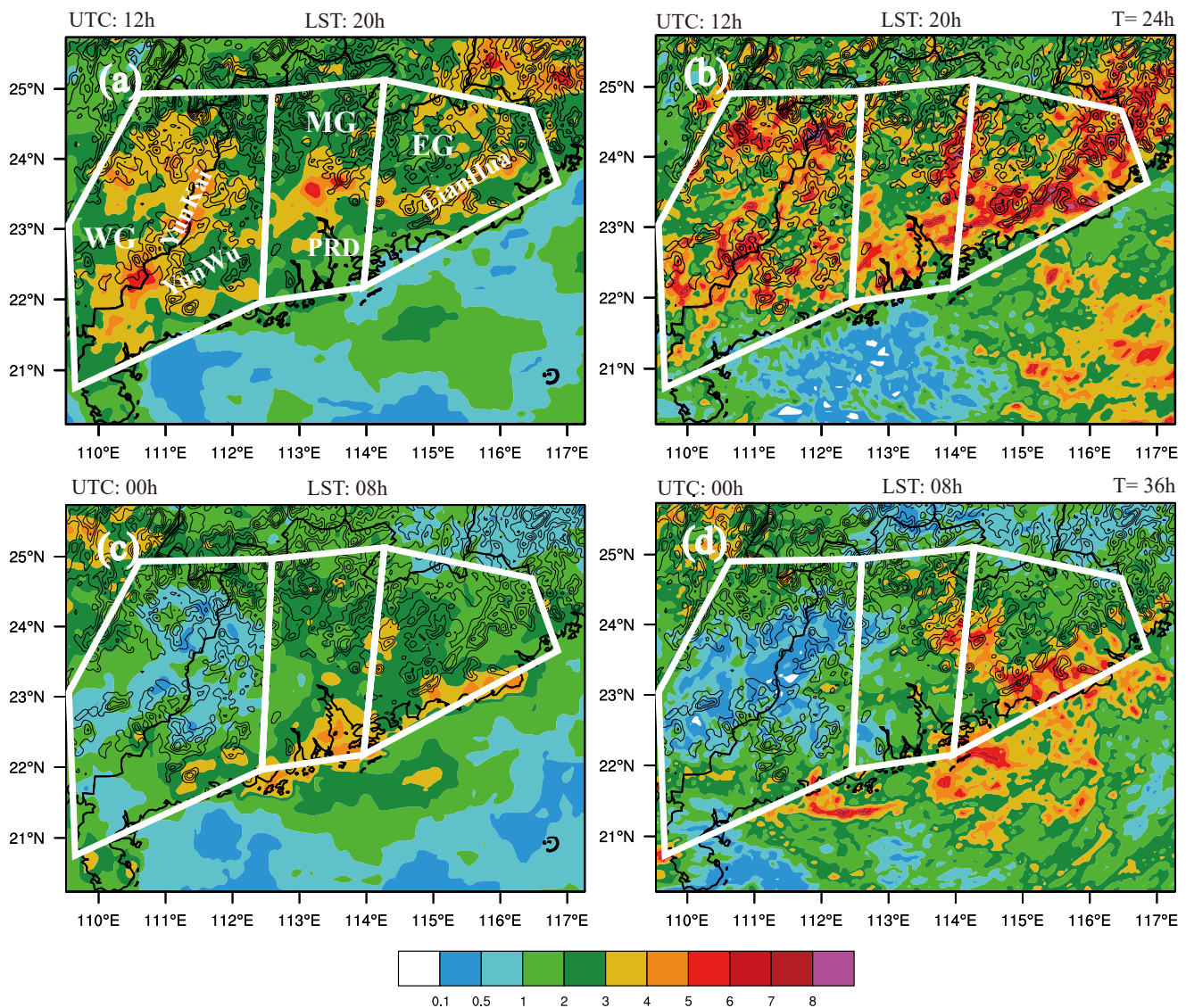


Figure 3. Mean six-hour accumulated rainfall from 1400 LST to 2000 LST during summer 2016 for (a) observations and (b) 4 km WRF forecasts. (c) and (d) are the same as (a) and (b) but for the early morning period from 0200 LST to 0800 LST. The thin black contours represent terrain height at 200 m intervals. “WG”, “MG” and “EG” represent western, middle and eastern part of the Guangdong Province, respectively.

Figure 4 shows a breakdown of the mean six-hour accumulated afternoon rainfall into average hourly rain rates. At 1400 LST, rainfall occurs over the inland mountains, the southern side of the western and eastern coastal mountains, and along the coastline. The WRF forecasts show a similar pattern but the intensity along the coastline and on the windward (south) side of the Lianhua Mountains of EG are clearly overpredicted. In addition, the precipitation in WG is underestimated. At 1600 LST, the observed rainfall over the YunKai Mountains is greatly enhanced as a result of solar heating. The WRF forecast successfully captures the variation of precipitation intensity over the YunKai Mountains, but the predicted intensity is clearly overpredicted. Also, the forecast produces excessive rainfall on the southern side of the coastal mountains, especially for EG. For MG, the precipitation propagates inland as the sea breeze and the mountain-valley breeze intensify. The observed precipitation center moves to the foot of the ^-shaped (see Figure 1a) mountains around 1800 LST (see Figure 4e). However, the forecast precipitation is mostly located in the vicinity of the coastline. At 2000 LST, the overall rainfall intensity is decreasing. The main rainfall is over the inland mountains and the southern side of the coastal mountains. The forecast shows a similar tendency and distribution, except for the PRD region, where scattered rainfall persists.

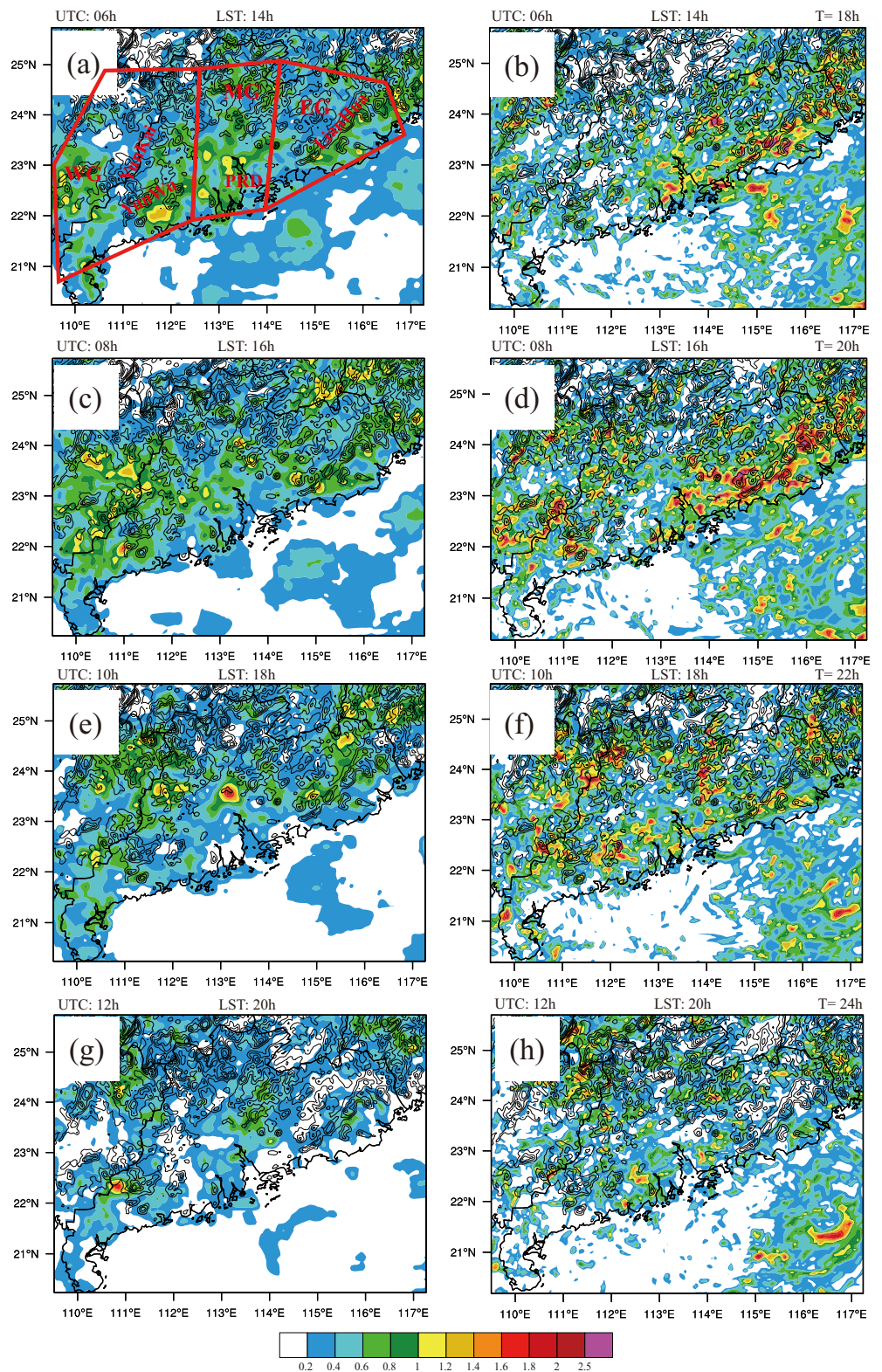


Figure 4. Mean hourly rainfall observed (left) and forecasted (right) during summer 2016. The rows are for 1400 LST, 1600 LST, 1800 LST and 2000 LST, respectively.

The rainfall variation during the early morning period is shown in Figure 5. The precipitation variations are not as obvious as the afternoon and are therefore shown at three-hour intervals. The observed rainfall is mostly along the coastline and gradually intensifies. In contrast, the forecast rainfall mostly forms over the ocean at 0200 LST and gradually extends to the coastline region around 0500 LST and further inland at 0800 LST. This reveals why the forecasts have precipitation mostly over ocean during the early morning period.

Overall, the WRF forecasts well capture the afternoon convection over the mountains and along the south side of coastal mountains. However, the intensity is clearly overpredicted, especially for rainfall over EG. Also, the predicted rainband has a clear position bias. During the afternoon period, the forecast rainband of MG is much closer to the southern coastline whereas the observations show a precipitation center a few hundred kilometers inland. By contrast, during the early morning period, the observed coastline rain is mostly located over land whereas the forecast rainfall is mostly over ocean.

3.2. Land-Sea Circulations and Their Correlation With Precipitation Propagation

Approximately 60% of convection initiation over southern China is concentrated within 100 km of the coastline (Bai et al., 2020a). The location and propagation of the associated rainfall systems are greatly influenced by the land-sea and mountain-plain circulations (Chen et al., 2016). In this subsection, we select two vertical slices within WG and MG to examine the land-sea and mountain-plain circulations and their impacts on the precipitation formation and propagation. A slice across EG show similar patterns to WG except that the vertical velocity is larger than that of WG, hence is not shown. The location of vertical slice may have some impact on the onset time of land/sea breezes but does not change the general conclusion. The fields examined are from the season mean forecasts of 4 km WRF; while there may be biases with the predictions, the general physical processes in the model should be qualitatively correct.

Figure 6 shows the mean winds at low levels and also the mean flows along lines AB and CD. The prevailing monsoon flows over southern China are southerly at 925 hPa and southwesterly at 850 hPa. The mean flows along AB and CD are prominently onshore at the low levels, though there are significant diurnal variations of onshore/offshore winds, as we will show later, especially at surface.

Figure 7 shows the wind component along line AB in Figure 6a and equivalent potential temperature at different times of the day, averaged over summer 2016. The wind component shown is the perturbation from daily mean. The fields show possible link between low-level winds and rainfall propagation. At 1400 LST, upslope winds (which first appear at 1000 LST, not shown) are established on the southern side of the coastal mountains. The precipitation (see red curve) is mainly located over the mountains and a few dozens of kilometers inland (the coastline is around 21.6°N). At 1600 LST, rainfall on the southern side of the coastal mountains is enhanced as the sea breeze penetrates further inland. It can be seen that the 362 K contour of equivalent potential temperature (θ_e) (black contours) rises over the mountains in late afternoon into evening (Figures 7b-d). High θ_e is due to either high temperature or high moisture. As will be shown later, temperature reaches its maximum at 1400 LST. Therefore, the increase of θ_e inland at low levels after 1400 LST is mainly from increase in moisture associated with the sea breeze. The relatively cold and moist air from the ocean serves to reduce low-level temperature and at the same time increases low-level moisture (this is confirmed by the temperature and moisture fields, not shown). This greatly increases the relative humidity and enhances cloud formation (van Stratum et al., 2014). The precipitation is enhanced on the southern side of the coastal mountains and new convection is also possibly generated as result of the interaction between the outflow of convection over the mountains and the sea breeze. At 1800 LST, the mean precipitation over land area reaches its maximum.

Into nighttime, the forecast precipitation first decreases and then gradually intensifies offshore. The consumption of water vapor by precipitation during the afternoon and the surface cooling at night greatly reduce θ_e . The 362 K θ_e contour gradually retreats back to the ocean (see Figure 7e-g). In the meantime, the land breeze begins to establish at around 2200 LST and extends to the ocean. At higher levels (up to 1.8 km as shown in Figure 7e and 6f), the direction of perturbation winds gradually turns inland. This change in the wind direction overnight at low levels can be well explained by the Blackadar's inertial oscillation theory (Du and Rotunno 2018; Xue et al., 2018). During the day, frictional effects in the boundary layer are increased by surface heating and boundary layer turbulence mixing. At night, as the frictional effect decreases as boundary layer becomes stable so that mixing dies out mostly, boundary layer wind speed increases and becomes super-geostrophic after midnight.

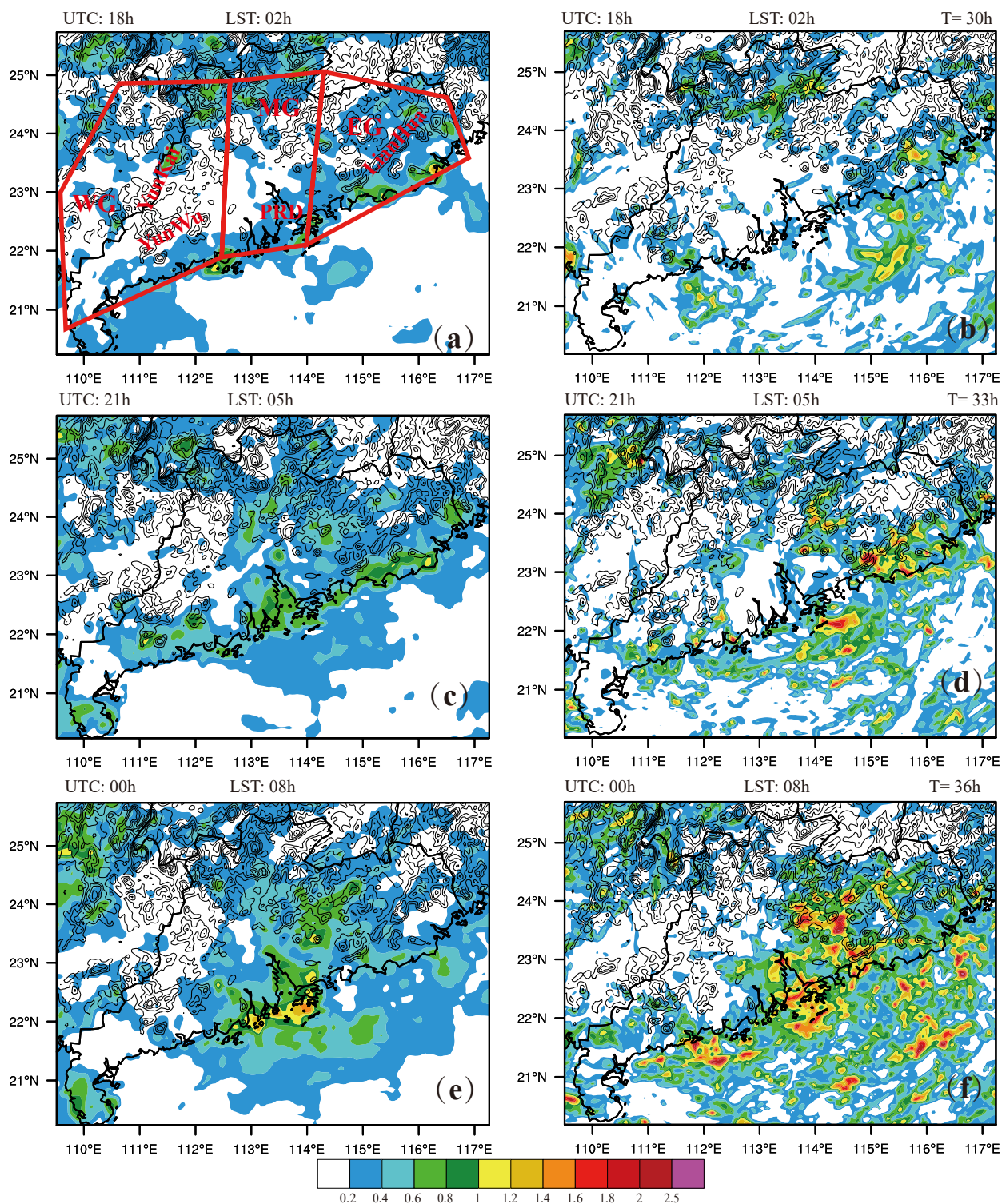


Figure 5. Same as Figure 4 but for the early morning period at (a) and (b) 0200 LST, (c) and (d) 0500 LST, (e) and (f) 0800 LST.

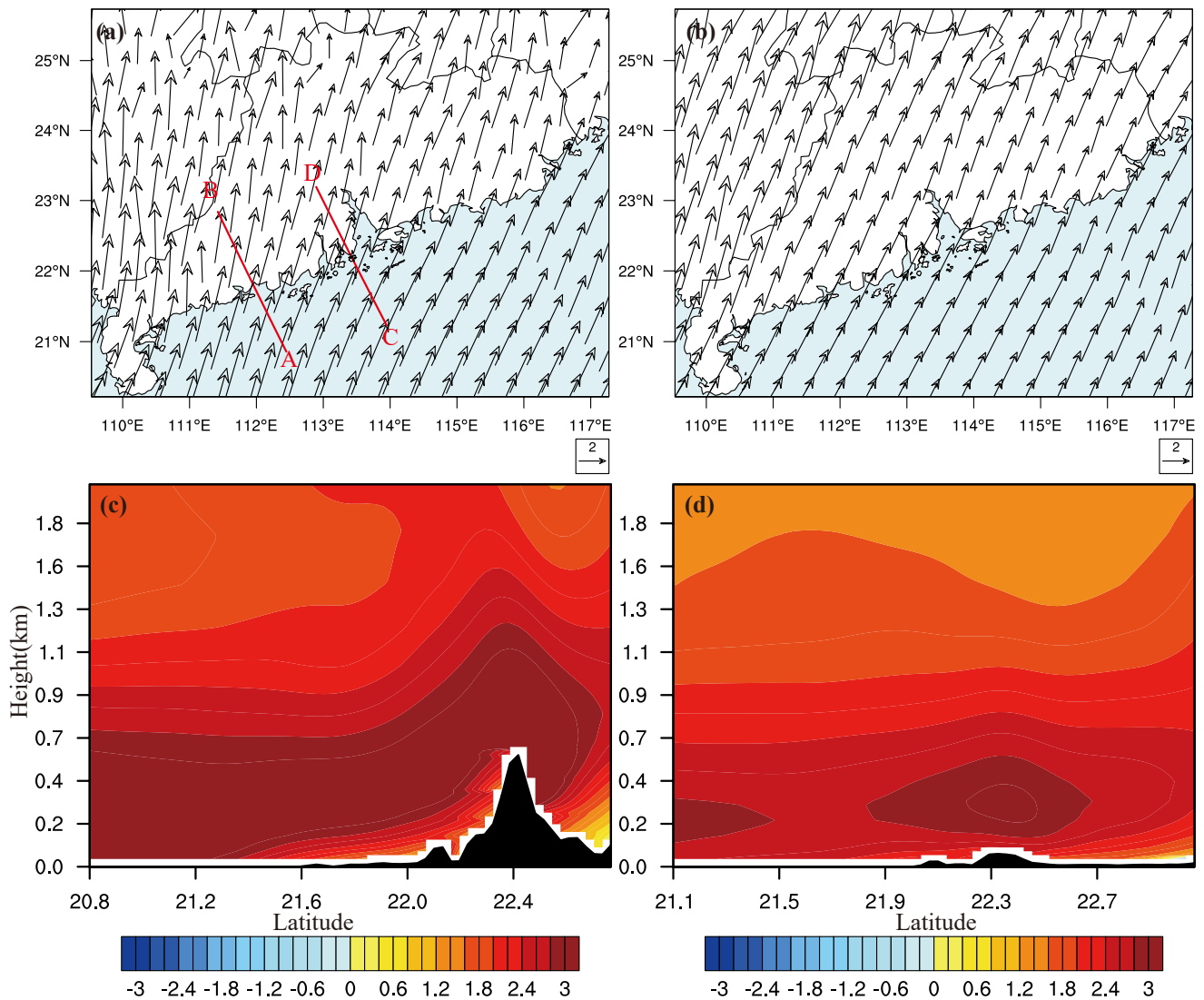


Figure 6. The mean prevailing winds during summer 2016, at (a) 925 hPa and (b) 850 hPa. Onshore (warm colors)/offshore (cold colors) wind speed in the vertical slice along lines AB (c) and CD (d) in (a), respectively.

The boundary layer wind vector (more accurately the ageostrophic wind vector) rotates clockwise due to inertial oscillation. The low-level wind reaches its maximum when the perturbation wind turns to the same direction as the prevailing (geostrophic) wind during the night. The onshore winds at the higher levels bring warm, moist sea air to the land. On the slope and at the foot of the southern coastal mountains, the air becomes potentially stable ($\frac{\partial \theta_e}{\partial z} > 0$), however, due to surface cooling and the warm-air layer above, suppressing convection inland. The precipitation forms offshore where the land breeze converges with the prevailing onshore winds and intensifies as the land breeze strengthens (see Figure 7e–g). The precipitation band then propagates inland with the prevailing winds. The mountain-plain breeze produced by the coastal mountains combines with the land breeze to enhance offshore convergence (Chen et al., 2016). The precipitation reaches its maximum intensity in early morning around 0800 LST (see also Figure 2).

Figure 8 shows another vertical slice (across line CD) to the west of PRD, where there is almost no high coastal terrain. The land-sea circulation is quite similar to that along line AB, except the onset time of onshore/offshore winds is postponed. It is not until 1400 LST that the sea breeze first appears (Figure 8b). The onset time of offshore winds is postponed to early morning at 0300 LST (see Figure 8f). It is noted that the onset time of sea breeze and land breeze in line AB is at 1000 LST and 2200 LST, respectively. A possible explanation is that the mountain-plain circulation produced by the coastal mountains may help strengthen onshore/offshore winds. We

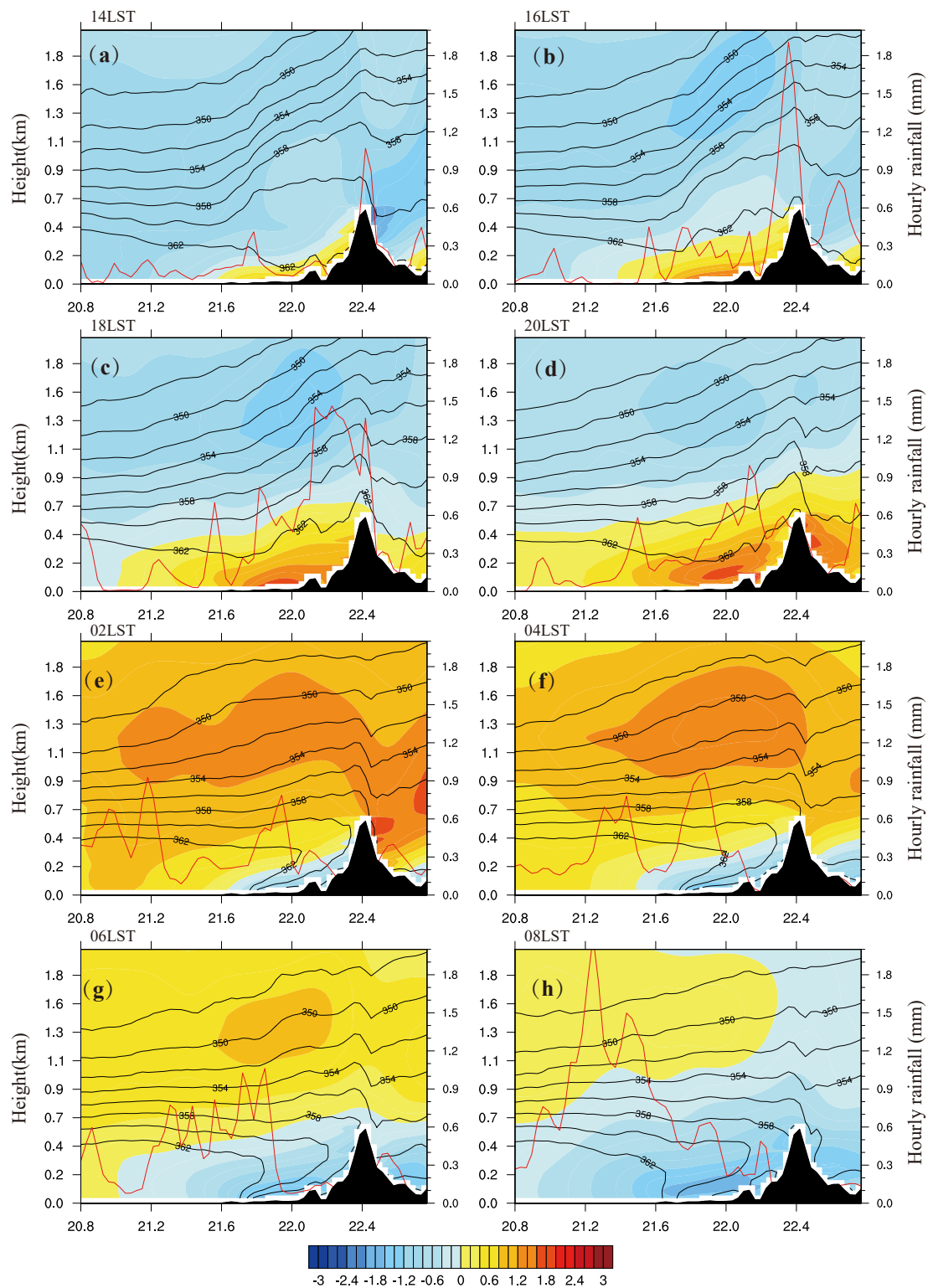


Figure 7. Cross-section of mean perturbation onshore (warm colored) and offshore (cool colored) winds, and equivalent potential temperature (black contours) during summer 2016 along line AB in Figure 6. The red line is the mean hourly precipitation (with vertical axis on the right side). The black shading is the terrain height. The left vertical coordinate is the altitude (km) and the right vertical coordinate is the precipitation amount (mm). The horizontal coordinate is the latitude along line AB.

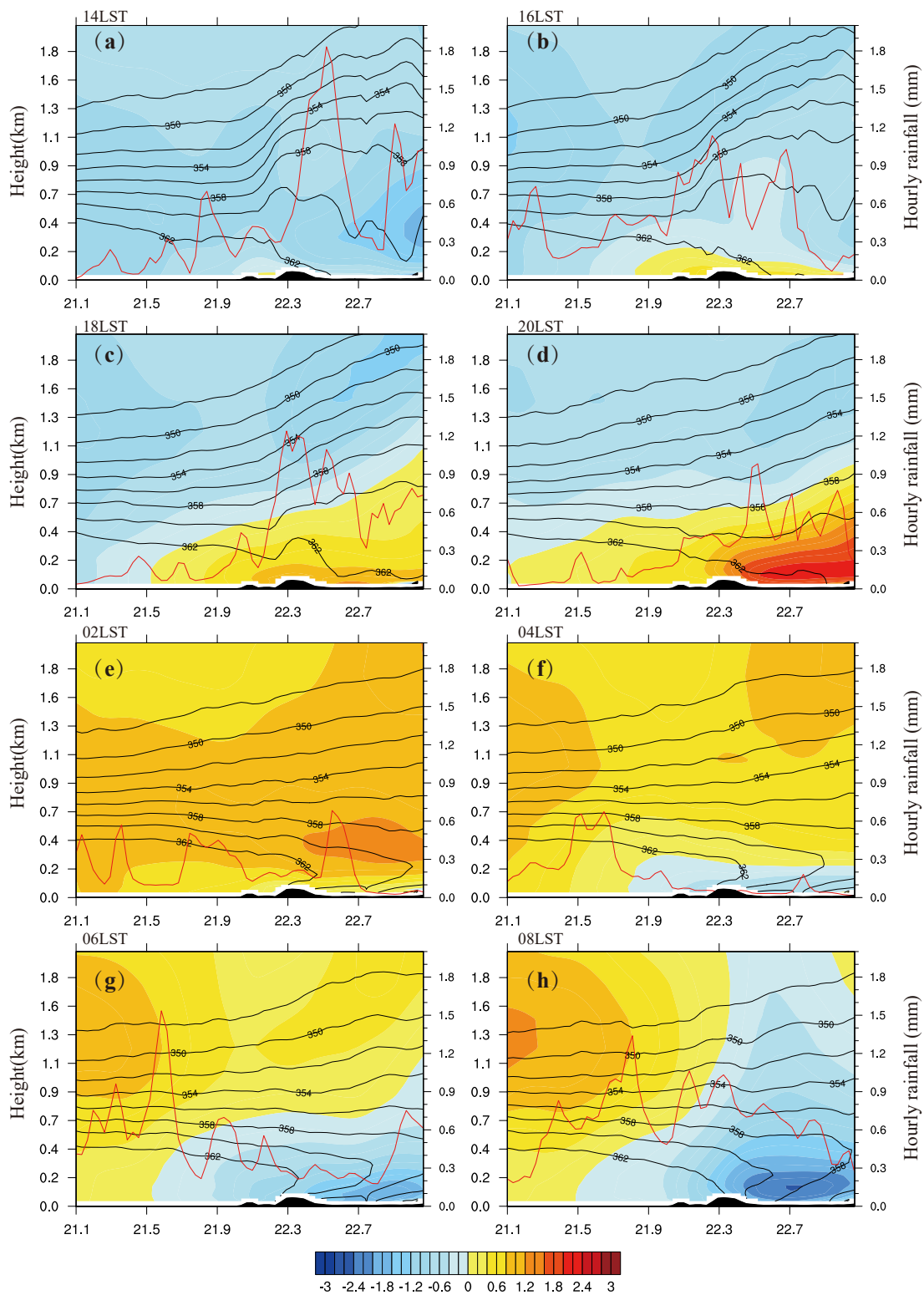


Figure 8. The same as Figure 7 but for the vertical slice across line CD in Figure 6.

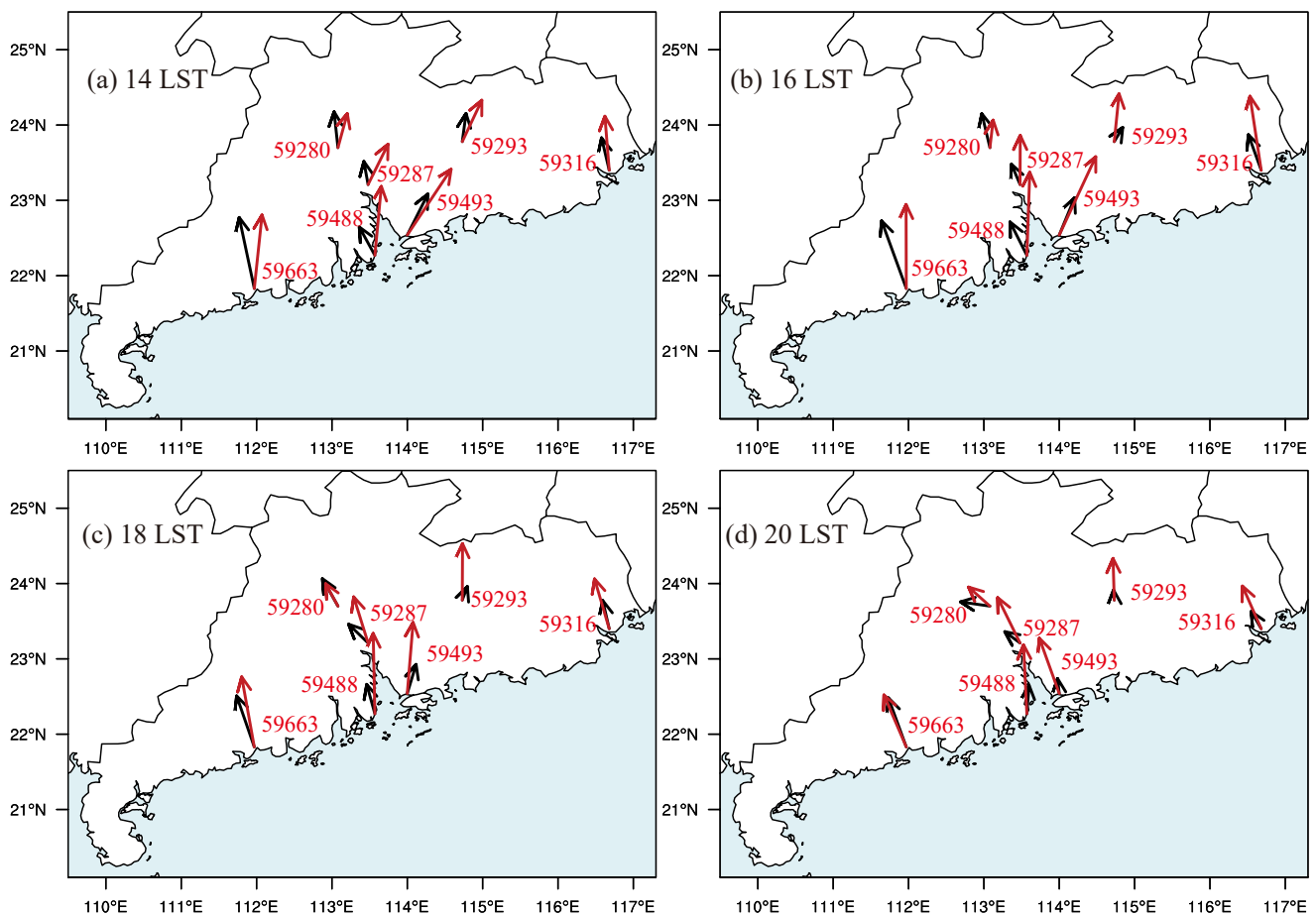


Figure 9. Mean surface winds for summer 2016 at (a) 1400 LST, (b) 1600 LST, (c) 1800 LST, and (d) 2000 LST. The black arrows represent sounding observations and the red arrows represent the WRF forecast.

also plotted several other vertical slices (not shown). The onset times of onshore/offshore winds are earlier in the western and eastern coastal mountains compared to PRD. Other possible explanations are related to Guangzhou city urban effect (Li et al., 2014) and the river delta region of PRD. These two factors can complicate local land-sea circulations. The exact reasons for the delay of onshore/offshore winds in PRD compared with other regions are beyond the scope of this paper. The precipitation propagation also has a close relation to land-sea circulations. The precipitation evolution along line CD is quite similar to that along line AB in Figure 6. During the afternoon, the precipitation forms along the coastline and propagates a few hundred kilometers inland. Overnight, the precipitation mostly forms and intensifies over ocean as the land breeze extends to the ocean. It propagates inland with the prevailing winds.

In summary, the land-sea circulations, aided by mountain-plain circulations, have substantial impacts on the location of precipitation, initiation, and subsequent propagation. Accurate prediction of the land-sea and mountain-plain circulations is essential for successful prediction of precipitation in southern China.

4. Factors Causing Precipitation Forecast Biases

4.1. Model Prediction of Low-Level Winds

The direction and speed of low-level winds are directly influenced by the land-sea circulations. In this subsection, we verify the forecast winds using surface and sounding observations. Figure 9 compares the mean forecast (red arrows) and observed (black arrows) 10 m surface winds at a number of surface station locations during the afternoon averaged over summer 2016. From 1400 LST to 1600 LST, the predicted winds at most sites show a clear eastward direction bias. In addition, the predicted wind speeds are generally higher than the observed wind

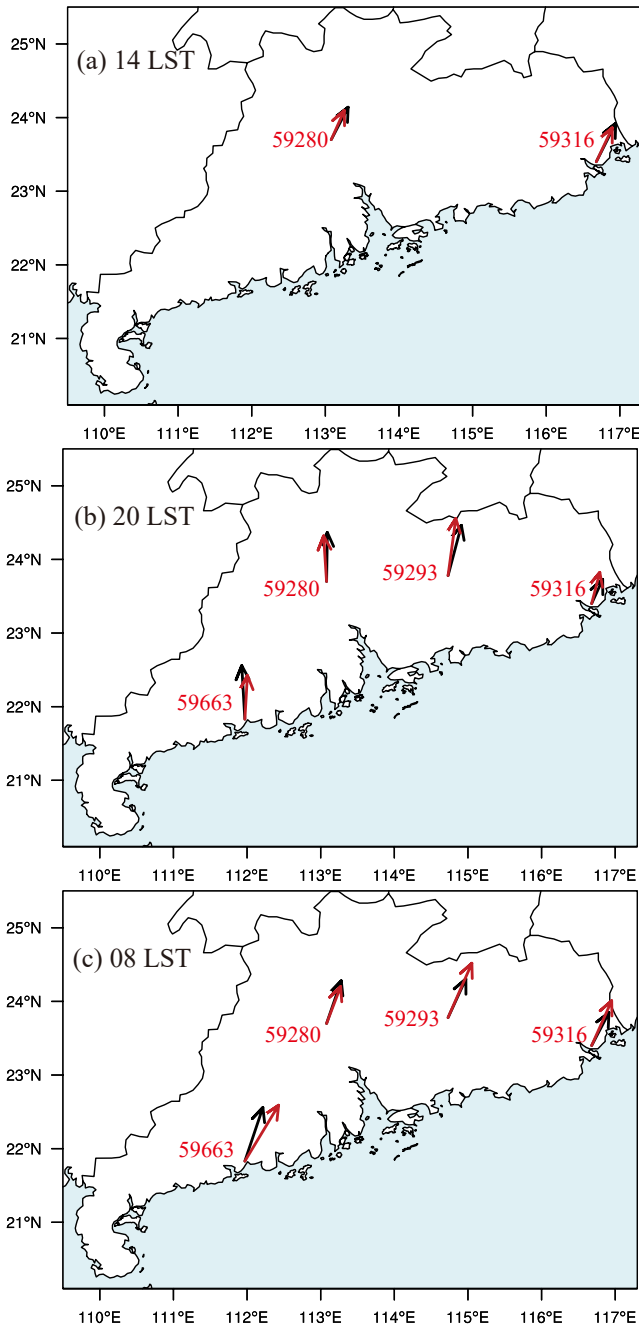


Figure 10. Mean wind vectors at 925 hPa during summer 2016 at (a) 1400 LST (0600 UTC, 18 h forecast length), (b) 2000 LST (1200 UTC, 24 h forecast length) and (c) 0800 LST (0000 UTC, 36 h forecast length). The black arrows represent sounding observations and the red arrows represent WRF forecasts. Note, that only two sites have sounding observations at 1400 LST.

speeds, except for two west most sites (59280 and 59663). The eastward wind direction bias in the upwind (more southwestern) locations allows more water vapor to be transported to EG and the high wind speed bias in the eastern regions enhances lifting on the southern side of coastal mountains. These two factors may explain the excessive rainfall over the eastern mountains and nearby regions in the WRF forecasts (Figure 4b, d). From 1800 LST to 2000 LST, as the predicted winds turn counterclockwise toward the west as in the observations (probably due to enhanced onshore sea breeze and mountain-plain circulations), the predicted rainfall begins to intensify in the western regions (see Figure 4d, f). However, the predicted wind speeds at most sites are still overpredicted, especially for the eastern sites located to the east of 113.2 °E. As the perturbation wind turns to the opposite direction of the prevailing wind during the night (due to land breeze and downslope winds), the wind speeds decrease rapidly in both forecasts and observations, and are close to zero, hence not shown.

To determine how well the model handles the wind prediction above the surface layer, Figure 10 verifies forecast winds against sounding observations at 925 hPa. At 1400 LST, only two sites have sounding observations. The forecasts match observations much better than at the surface at 1400 and 2000 LST. At 0800 LST (36 h forecast length), the predicted winds show similar wind directions as observations except an eastward bias at the upwind site 59663. Overall, the forecast upper air winds are generally reliable.

Figure 11 shows hodograph of 10 m winds from four surface stations along the southern coastline (see Figure 1). Two sites are located on the west/east coastline where there are coastal mountains within a hundred kilometers, and two on the southwest/southeast corners of the PRD region. The hodograph for the surface wind observations and forecasts from 0800 LST (12 h forecast length) to 0700 LST of the following day (35 h forecast length) are shown. The observations (black lines) show mostly anticlockwise rotation, except for the south-west corners of the PRD (59488). The anticlockwise/clockwise rotation is determined by the pressure gradient and Coriolis force at the surface (Alpert et al., 1984; Romine et al., 2018). The topography often complicates the rotation (Simpson, 1996). Being on the coastline, the diurnal variations of winds at the four sites are strongly influenced by land-sea breezes, with additional modulation by mountain-plain circulations for sites close to mountains. The effect of boundary layer inertial oscillation appears to have smaller effects at these sites.

The forecasts (red lines) successfully reproduce the observed clockwise/anticlockwise rotation, indicating that the overall diurnal variations of land-sea and mountain-plain circulations are correctly simulated. However, the predicted wind speed, amplitude of variations (the difference between the maximum west (south) and east (north) winds), and the onset time of onshore/offshore winds (the time when winds turn toward land/sea) are not the same as observations. The wind speeds are overpredicted throughout the day for the two sites within the PRD region. For site 59663 (located in WG), from 1000 LST to 1900 LST, the observed wind direction turns inland (onshore winds). After that, the wind direction gradually turns toward the ocean. In the forecast, it is not until 1200 LST that the predicted wind direction turns toward land. In addition, the onset time of offshore winds is also delayed for about an hour (Figure 11a). Another clear difference is that the predicted north-south (v) wind component turns toward the south a few hours before 0800 LST, although the speed is quite low. The same occurs for site 59316 in EG. As explained later, this is because the land breeze is overpredicted.

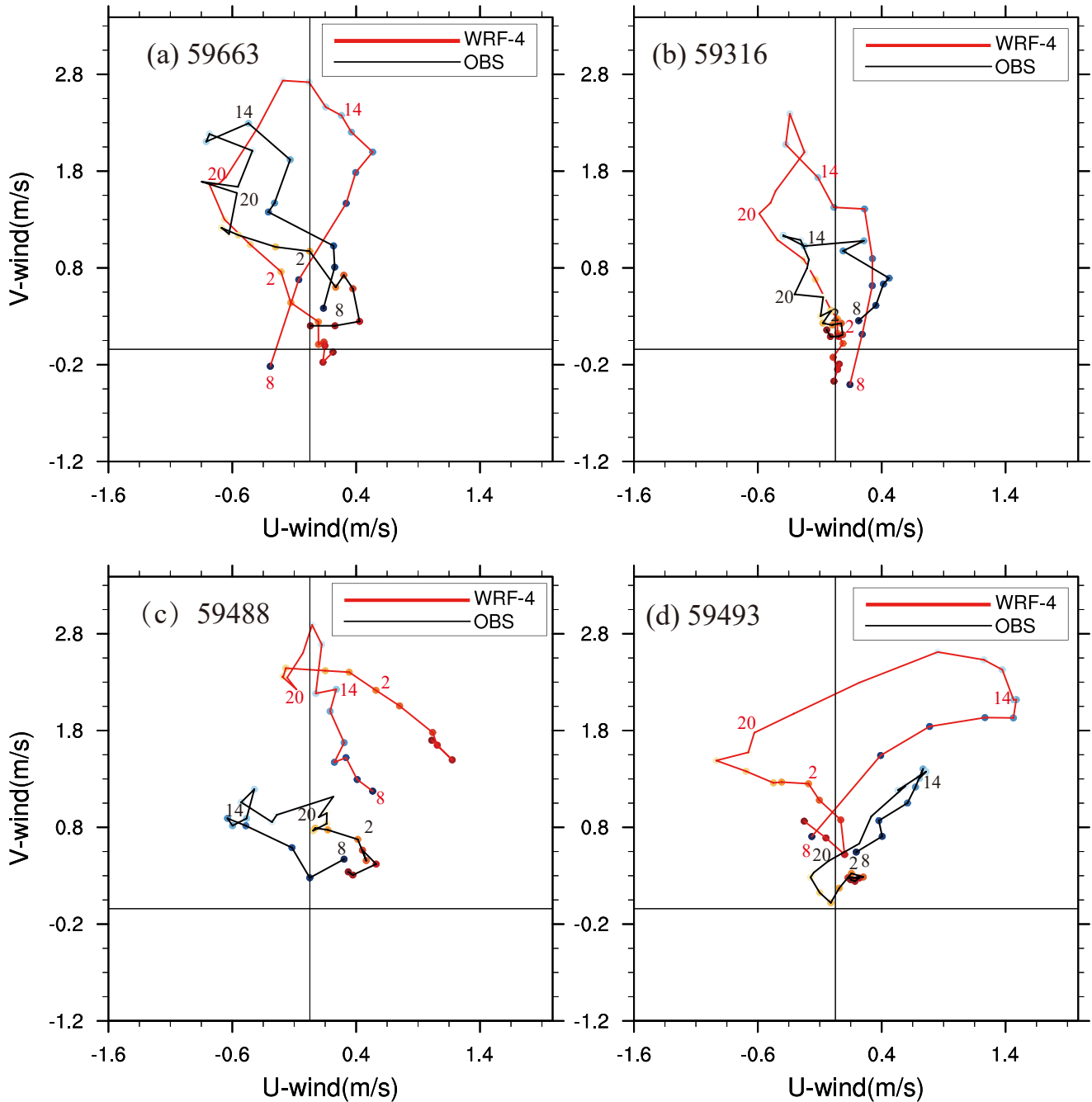


Figure 11. Hodograph of the observations and WRF forecasts from 12 to 36 h of forecast at surface for sites (a) 59663, (b) 59316, (c) 59488, and (d) 59493. The numbers indicate the local solar time. The sites location are marked in Figure 1.

A stronger land breeze explains why the predicted coastline rain belts penetrate deeper into the ocean (see Figure 3b, d, and Figure 5).

In general, the model can handle the variations of land-sea and mountain-plain circulations, but with biases in the onset time of changes and in wind intensity. The surface winds show a systematic eastward bias during the afternoon. Furthermore, the land breeze seems to be overpredicted for the western and eastern coastline during the early morning. These systematic forecast biases in wind direction and speed can result in errors in the timing, distribution, and propagation of rainfall.

4.2. Model Prediction of Land-Sea Contrast

The land-sea circulations are largely determined by the land-sea thermal contrast (Hu & Xue 2016). Figure 12 compares the CLDAS analysis (left) and forecast (right) summer mean surface temperature. The observed temperature reaches its maximum at 1400 LST (see also Figure 13a). After that temperature begins to decrease. A clear urban heat island is observed in the PRD region throughout the night (see Figure 12c, e, and g). Typically, nocturnal urban heat island persists throughout night (Hu & Xue 2016). The observed temperature within PRD is about 2 K higher than the surrounding regions. For the forecast, the temperature over land is clearly underestimated (see also Figure 13a). There is no significant temperature difference between urban and rural areas (see Figure 12g, f, h).

There are several possible explanations for the cold bias in WRF forecasts over land. First, the GFS initial condition fields underestimate the land surface temperature over southern China. There is about average 1.2 K negative bias (not shown) over land and that negative bias is maintained throughout the forecasts. Second, except for land cover types, the current model does not include special treatments for urban effects (Hu et al., 2013). Rapid urbanization over the region causes the land cover and its related land-surface properties not up to date in the model, and is probably one of the reasons for the poor performance in the region (Li et al., 2014). Figure 1b shows that only a small fraction of the region is categorized as urban and built-up lands (red color) in the region. This is almost certainly incorrect and will likely result in large temperature biases because the surface albedo and surface exchange parameters will be incorrect. And the 4 km WRF fails to predict the urban heat island effects (Figure 12g, f, h). Third, deficiencies with the PBL scheme and land surface model can also cause error in forecast near surface conditions. The predicted temperature drops abruptly around 2000 LST (Figure 13a) and cold bias persists throughout the night. The abrupt temperature decrease around sunset may be caused by deficiencies of the PBL scheme. Specifically, during the transition period from the unstable afternoon boundary layer to the nocturnal stable condition, the vertical turbulent mixing coefficient of the PBL scheme undergoes a rapid drop (Hu et al., 2010; Zheng et al., 2017). Weak turbulent mixing is unable to mix cold air upwards, leading to excessive cooling of the surface temperature during this transition period. Figure 14 shows the profile of simulated potential temperature and sounding observations at 20 LST. Compared to observations, the forecasts show more stable vertical temperature gradients at low levels, consistent with suppressed vertical mixing.

Compared with the temperature over land, the difference between forecasts and CLADS analyses is relatively smaller over ocean, with no more than 0.5 K (see Figure 13b). The diurnal variation of temperature is also small. The difference between the maximum and minimum mean temperatures over ocean is less than 1 K (Figure 13b). In contrast, over land, the diurnal variation of 2-m temperature reaches ~ 7 K in forecasts (Figure 13a). Thus, the land-sea thermal contrast is largely determined by the variation of temperature over land.

Figure 13c also shows the temperature difference between land and sea. To remove the impact of coastal mountains, all temperatures are corrected to sea-level height using a temperature lapse rate of 6.5 K per km. In addition, the sea (land) area is excluded for the calculation of mean temperature over land (sea) area. During the day, the model underestimates land-sea thermal contrast. During the night, owing to the excessive cooling over land, the model overestimates land-sea thermal contrast in terms of magnitude. The systematic land-sea thermal contrast bias results in a weaker sea breeze during the day but a stronger land breeze during the night. Land-sea circulations are the major source of wind variations at the surface near the coast. Since the mean prevailing winds at the surface are southwesterly, a weaker sea breeze normal to the southwest-northeast oriented coastline could be responsible for the systematic eastward bias for the mean winds during the afternoon (Figure 9). A stronger land breeze is likely the reason for the predicted offshore winds at the coastline sites (59663 and 59316) during early morning hours (Figure 11a, b). It is noted that the high wind speed bias for sites 59488 and 59493 located at the south-west and south-east corners of the PRD region is due to the overprediction of mean prevailing winds. If we look at the variation of wind direction, the forecast in the south-west corner (59488) shows clockwise rotation, whereas in the south-east corner (59493) shows an anticlockwise rotation. The PRD delta region causes an almost opposite perturbed pressure gradient at the two sites, which is also the reason for the different rotation directions (clockwise/anticlockwise) at these two sites (see Figure 11c, d). Overall, the model significantly underpredicts the surface temperature over land, especially during the night, which in turn leads to inaccurate land-sea circulations and systematic biases in forecast surface winds.

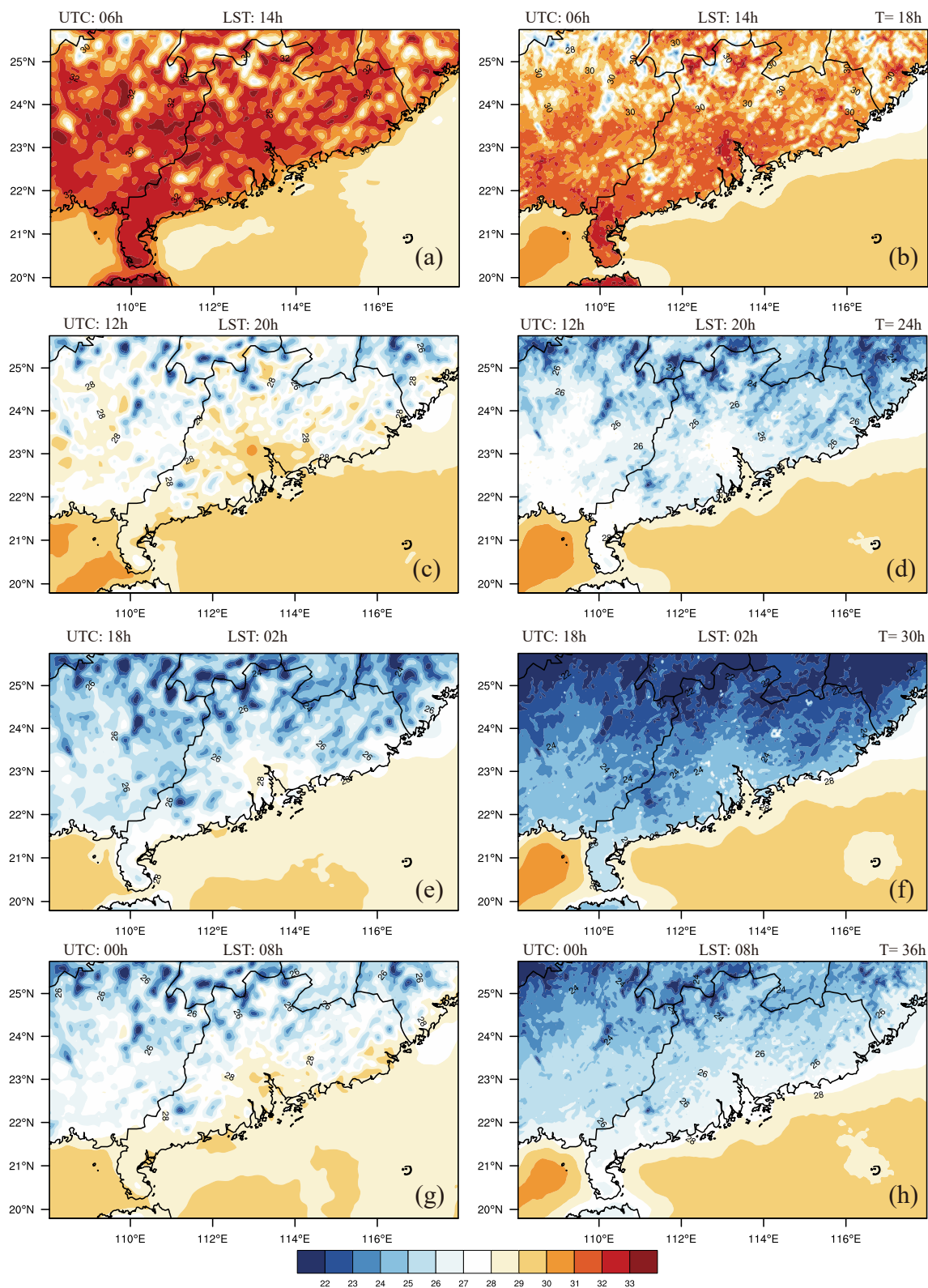


Figure 12. The observed (left) and 4 km WRF forecast (right) surface temperature at (a) and (b) 1400 LST, (c) and (d) 1600 LST, (e) and (f) 1800 LST, (g) and (h) 2000 LST.

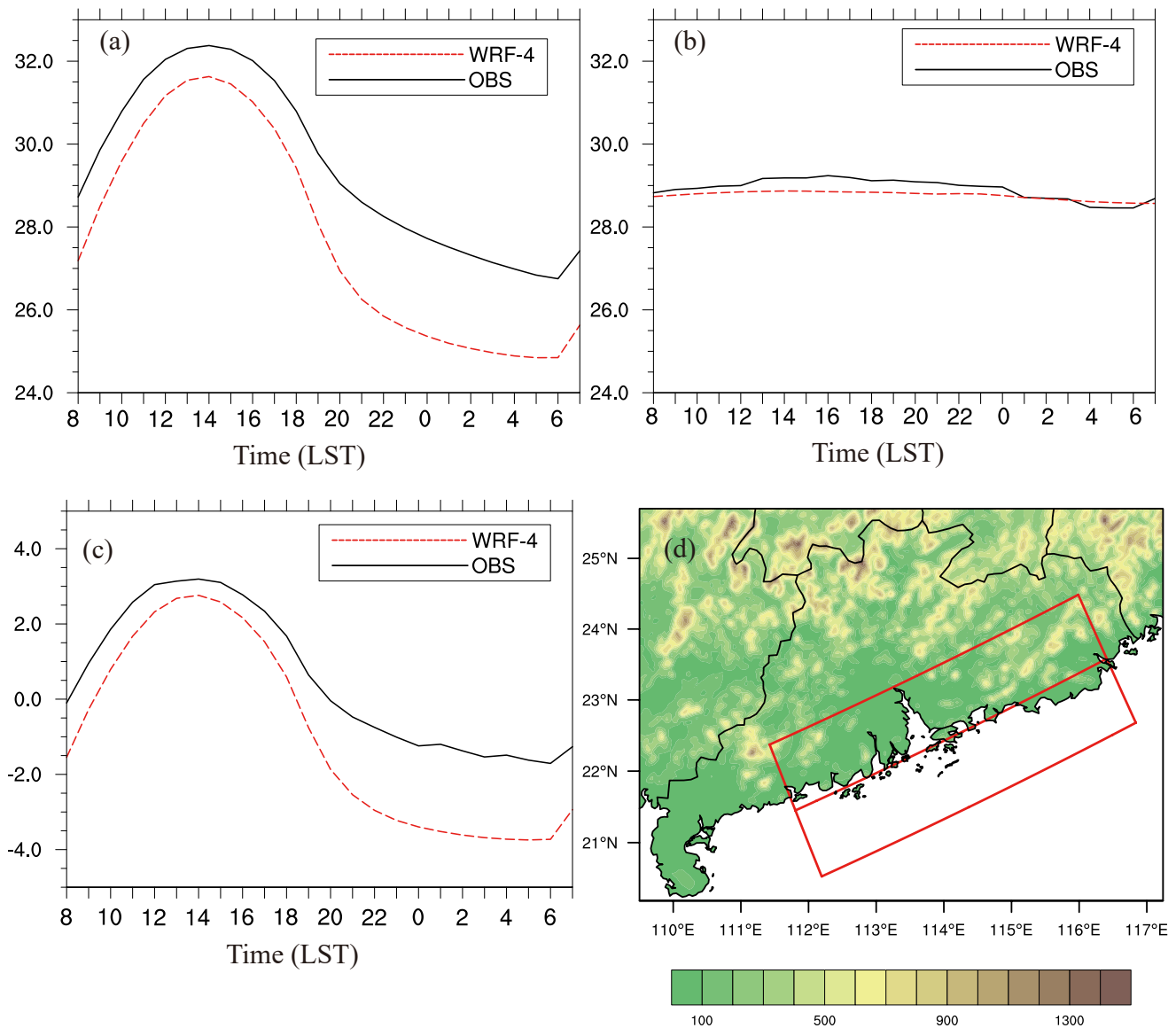


Figure 13. (a) Averaged 2m temperature over land side in the red rectangle of (d) during the summer 2016. (b) Same as (a) but for the ocean side. (c) The land-sea thermal contrast. (d) shows where the red box. Here, the temperature are all corrected to sea level. Also, the sea (land) points are excluded during the calculation of mean surface temperature of land (sea) area.

4.3. Model Prediction of Low-Level Moisture

As pointed out earlier, overprediction of rainfall intensity over southern China is a major issue in the 4 km WRF forecasts, especially near the southern coastline (see Figure 3). The microphysics scheme used may be responsible for some of the overprediction (Zhu & Xue 2016). The Morrison double-moment scheme used tends to overestimate the raindrop size while the number concentration is close to observations. This can result in excessive rainfall, especially for heavy rainfall (Furtado et al., 2018; Zhu et al., 2018a). Bias in low-level moisture can have even more impact on precipitation forecast, as we will see next.

Figures 15 and 16 compare forecast water vapor mixing ratios at 850 hPa, 925 hPa, and the surface to NCEP FNL analyses. The difference between the WRF forecasts and FNL analyses may be mostly due to boundary and surface layer physics in the model. Overall, the forecasts overpredicted low-level water vapor content. This is also confirmed by comparing the forecast with the sounding observations (not shown). Over land, the forecast overestimates water vapor content at low levels. The longer the forecast range, the larger is the difference between

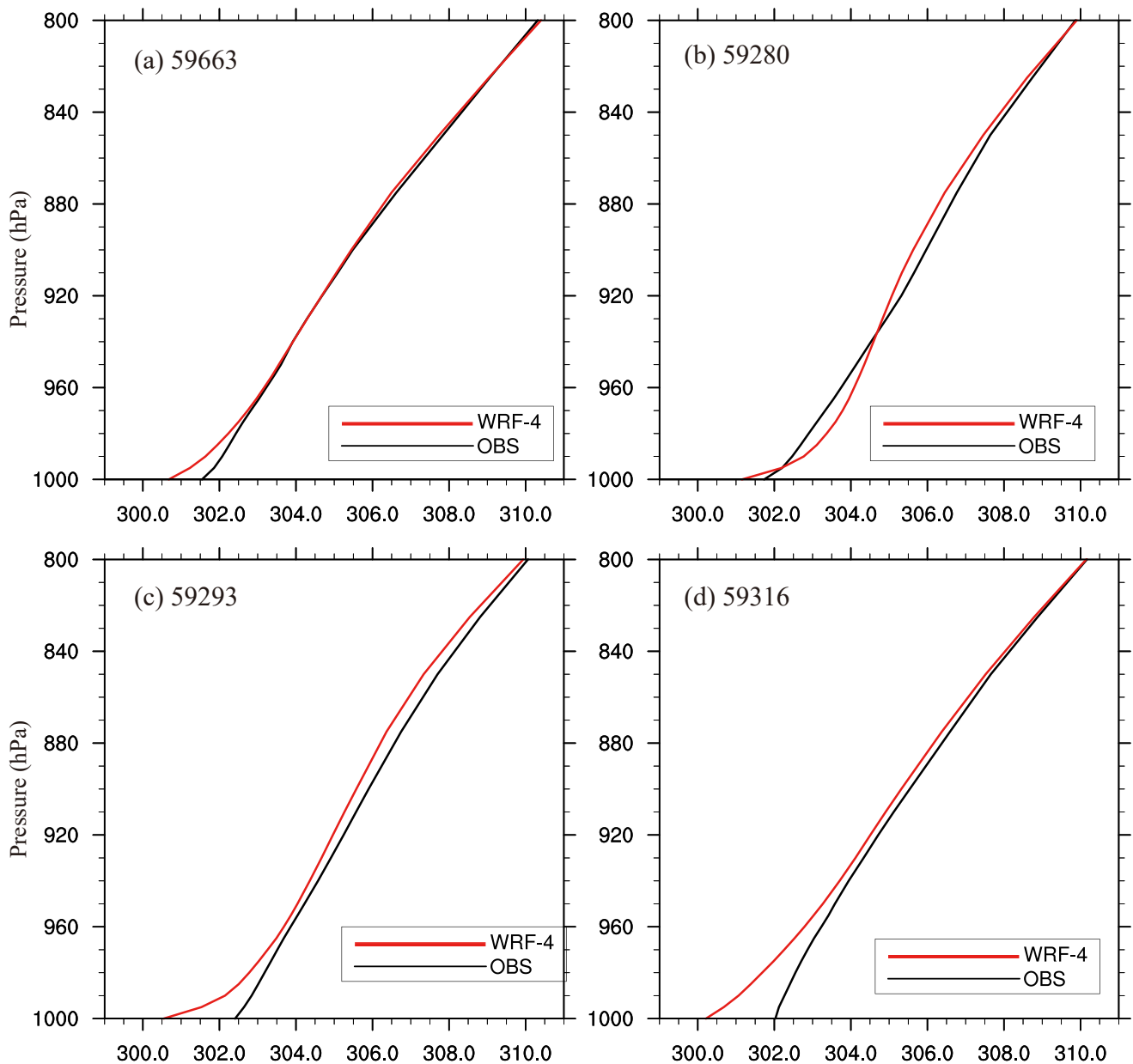


Figure 14. Potential temperature of WRF 24 h forecasted and sounding observations at 20 LST during the summer 2016 for the sites (a) 59663, (b) 59316, (c) 59488, and (d) 59493.

FNL analyses and forecasts. At 1400 LST (18 forecast hours), the forecast water vapor is clearly higher than that in FNL, especially for the southern slope of the coastal mountains (see Figure 15c, d) and over ocean (see Figure 15e, f). The difference over ocean at the surface becomes more obvious around sunset (see Figure 16e, f). The predicted water vapor over ocean is about 2 g kg^{-1} higher than that of FNL at 2000 LST, whereas this difference is about 1 g kg^{-1} for most of the ocean area at 1400 LST. Too much moisture fluxes from the ocean surface should be the main cause. One possibility is that the surface exchange coefficient of moisture fluxes is not accurately parameterized in the PLX surface layer scheme. Due to the lack of detailed observations over the ocean, the exact cause is uncertain and is a subject for future investigation. In any case, the significant high bias in forecast low-level moisture over the ocean is an important reason for the overprediction of rainfall amount over southern China.

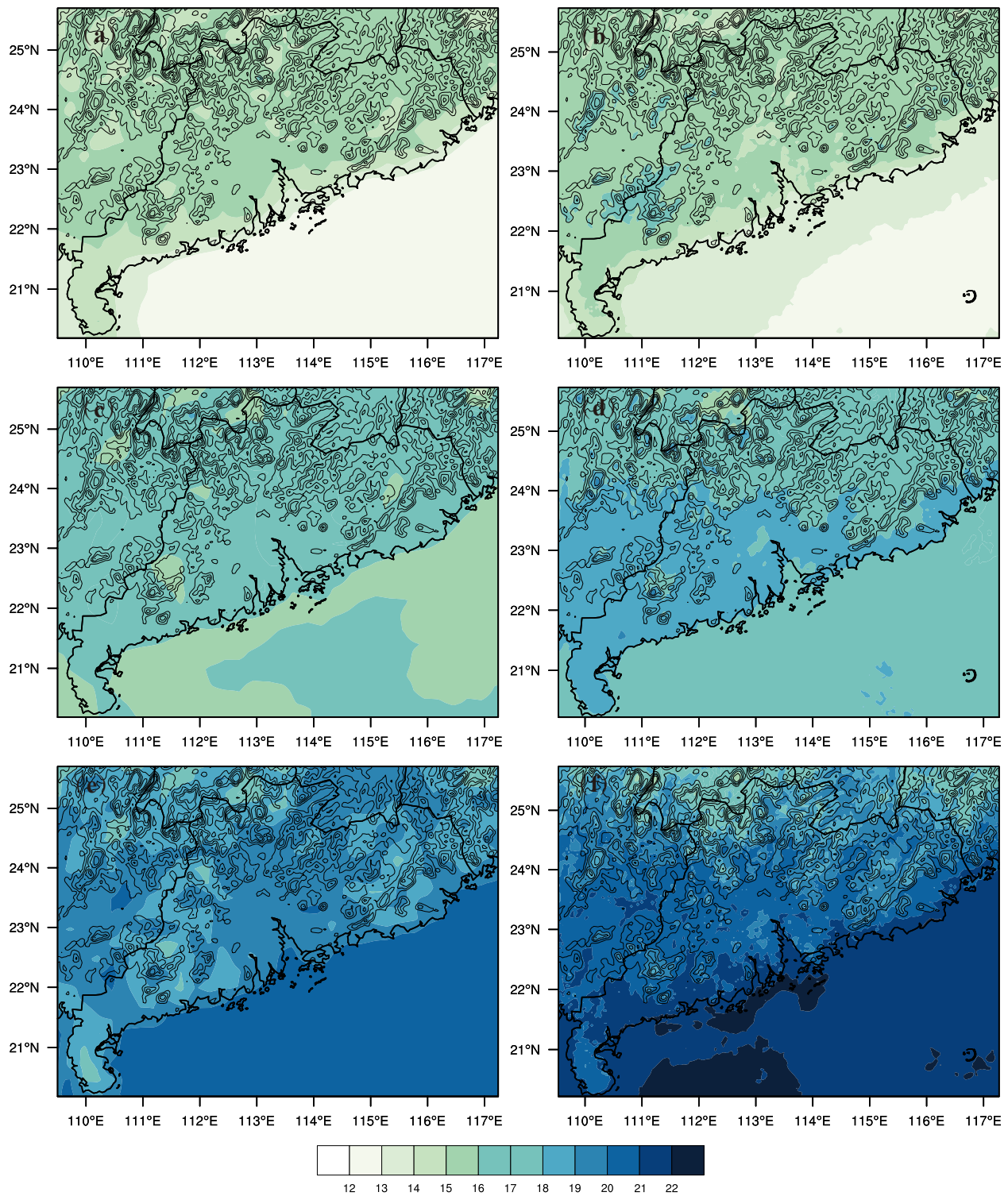


Figure 15. The mean water vapor mixing ratio during summer 2016 for the NCEP FNL observations at (a) 850 hPa, (c) 925 hPa, and (e) the surface; (b), (d), and (f) The same as (a), (c), and (e) but for the 4 km WRF forecast. The observation time is at 1400 LST. The thin black contours represent terrain height at 200 m intervals.

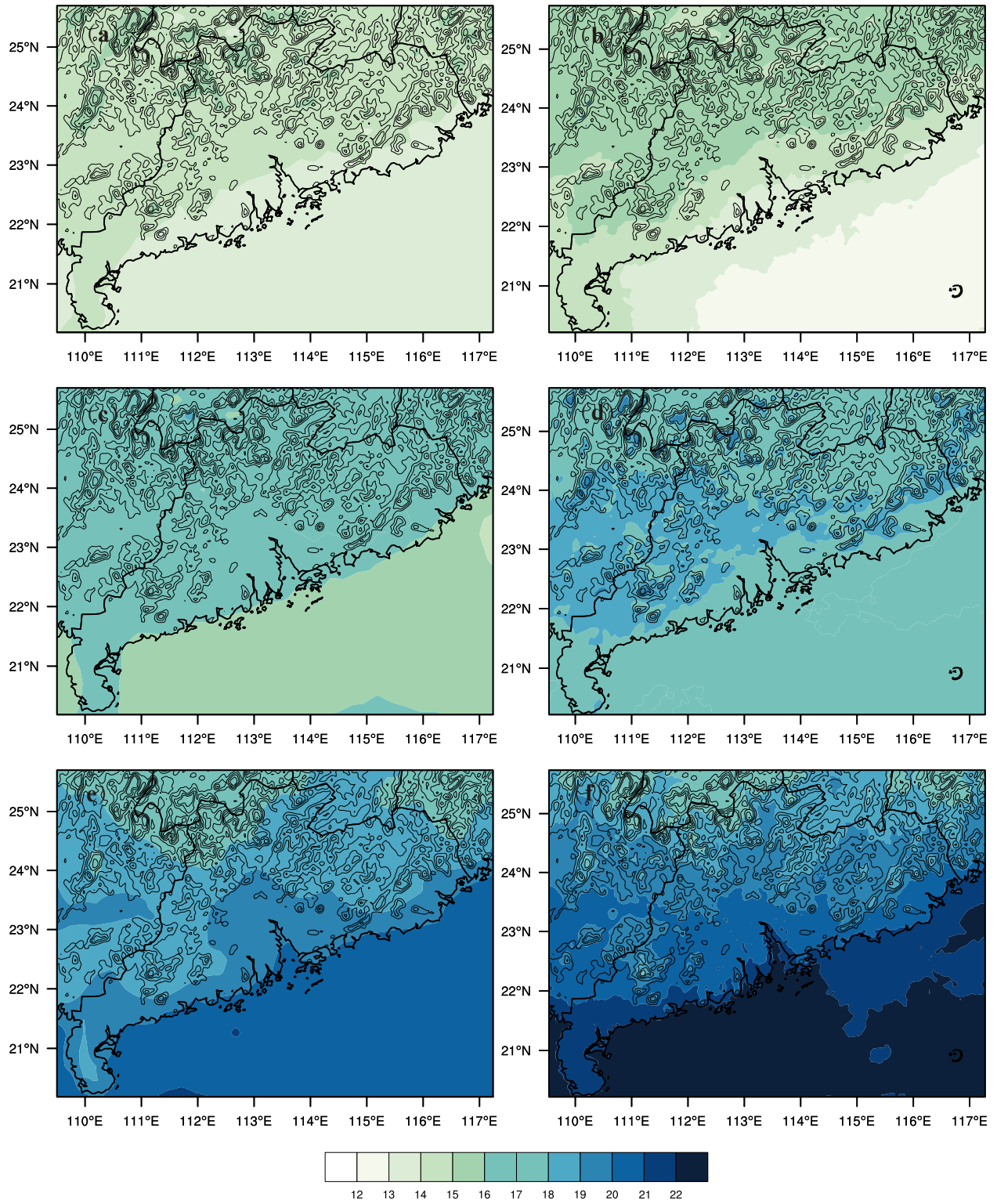


Figure 16. The same as Figure 15 but at 2000 LST.

5. Summary and Future Work

In our previous study, we evaluated the performance of real-time 4 km WRF model forecasts over China during the summer season (Zhu et al., 2018a). Biases in forecast rainfall over southern China were noticed: the location of predicted rainfall is shifted off to the southeast and the rainfall intensity is significantly overpredicted. In this study, we explore the possible factors that lead to such precipitation forecast biases. The forecasts during summer 2016 are examined. We mainly focus on investigating low-level state variables that have direct impacts on the land-sea and mountain-plain circulations and moisture supply. The biases in these variables and their relationship with the precipitation forecast biases are inferred.

Over southern China, especially near the coastline, land-sea circulations play important roles in the formation and propagation of precipitation systems. Owing to high thermal instability and moisture content, together with coastal topography, moist convection often forms even under weak synoptic conditions. Accurate prediction of low-level conditions such as the land-sea circulations is critical to successful precipitation forecast in the region. Compared with observations, the predicted surface winds have a clear eastward bias during the afternoon. This explains why the forecasts show a higher rainfall amount over the eastern part of Guangdong Province than over the western part. Further investigation of the land-sea thermal contrast shows that the underprediction of daytime surface temperature over land is the reason for the weaker onshore winds. The cold bias over land results in weaker land-sea thermal contrast during the day, which in turn leads to weaker sea breeze and eastward wind bias. The cold bias over land is greatly increased around sunset and persists throughout the night. As a result, the predicted land breeze is stronger than observed, pushing more precipitation off to the ocean at night.

In addition, we investigate the accuracy of low-level moisture in the forecast. Compared to reanalysis, the water vapor content is clearly overpredicted over southern China, especially near the southern slope of the coastal mountains and over ocean. The moist bias is mainly near the surface. The high moisture bias over the ocean that increases with forecast range indicates that the ocean surface moisture fluxes are overestimated, and too strong surface winds and error in drag coefficient parameterization are suspected to be the causes. The high moist bias is another important reason for the overprediction of the precipitation over the coastal regions in southern China.

The current study tries to give the most likely explanations for the biases in precipitation forecasts in the southern China, but they likely do not cover all possible sources of error. For example, in addition to error in the magnitude of diurnal wind variations, we also notice that the average prevailing wind speed in PRD is overpredicted over land. However, the reason is still not clear. Also, the large cold bias over the PRD is believed to be related to the outdated land-use information in the USGS data set used in the forecasts. To what extent and how the land cover may affect the temperature forecast and wind circulation over cities and their surrounding area require further study. Besides, the overestimation of rainfall may lead to negative bias in surface temperature forecast. The interaction between temperature and precipitation also needs further investigation. In the future, we plan to carry out sensitivity experiments to better answer some of the questions, including the use of different parameterization schemes. The current large forecast domain, 4 km over entire China, requires significant computational resources, especially when run over full seasons. Representative cases where systematic biases are noticed can be used to do the investigation first. To better evaluate/verify forecasts of land and ocean surface conditions, and associated fluxes, better observations will be needed. Some of them are available from special field experiments, and such data should be fully utilized for the benefit of understanding and improving physics parameterizations. These are subject for future studies.

Data Availability Statement

The CLDAS land surface analysis data, surface, sounding observations, and as well as the hourly precipitation observation could be obtained from the website: <http://data.cma.cn/>. The NCEP 0.25°×0.25° FNL are available at <https://rda.ucar.edu/datasets/ds083.3>. The size of original WRF forecasts is very large. Anyone who is interested could request selected variables via email zhukf@cma.gov.cn.

Acknowledgments

This work was primarily supported by the National Key Research and Development Program of China under grant 2018YFC1507604 and the National Natural Science Foundation of China (Grant No. 41975124).

References

- Alpert, P., Kusuda, M., & Abe, N. (1984). Anticlockwise Rotation, Eccentricity and Tilt Angle of the Wind Hodograph. Part II: An Observational Study. *Journal of the Atmospheric Sciences*, *41*, 3568–3583. [https://doi.org/10.1175/1520-0469\(1984\)041<3568:areata>2.0.co;2](https://doi.org/10.1175/1520-0469(1984)041<3568:areata>2.0.co;2)
- Bai, L. Q., Chen, G. X., & Huang, L. (2020a). Convection Initiation in Monsoon Coastal Areas (South China). *Geophysical Research Letters*, *47*. <https://doi.org/10.1029/2020gl087035>
- Bai, L. Q., Chen, G. X., & Huang, L. (2020b). Image Processing of Radar Mosaics for the Climatology of Convection Initiation in South China. *Journal of Applied Meteorology and Climatology*, *59*, 65–81. <https://doi.org/10.1175/JAMC-D-19-0081.1>
- Chang, C.-P., Hou, S. C., Kuo, H. C., & Chen, G. T. J. (1998). The Development of an Intense East Asian Summer Monsoon Disturbance with Strong Vertical Coupling. *Monthly Weather Review*, *126*, 2692–2712. [https://doi.org/10.1175/1520-0493\(1998\)126<2692:tdoae>2.0.co;2](https://doi.org/10.1175/1520-0493(1998)126<2692:tdoae>2.0.co;2)
- Chang, H.-L., Brown, B. G., Chu, P.-S., Liou, Y.-C., & Wang, W.-H. (2017). Nowcast Guidance of Afternoon Convection Initiation for Taiwan. *Weather and Forecasting*, *32*, 1801–1817. <https://doi.org/10.1175/waf-d-16-0224.1>
- Chen, H., Yu, R., Li, J., Yuan, W., & Zhou, T. (2010). Why Nocturnal Long-Duration Rainfall Presents an Eastward-Delayed Diurnal Phase of Rainfall down the Yangtze River Valley. *Journal of Climate*, *23*, 905–917. <https://doi.org/10.1175/2009jcli3187.1>
- Chen, X., Zhao, K., & Xue, M. (2014). Spatial and temporal characteristics of warm season convection over Pearl River Delta region, China, based on 3 years of operational radar data. *Journal of Geophysical Research: Atmospheres*, *119*, 2014JD021965. <https://doi.org/10.1002/2014jd021965>
- Chen, X., Zhang, F., & Zhao, K. (2016). Diurnal Variations of the Land–Sea Breeze and Its Related Precipitation over South China. *Journal of the Atmospheric Sciences*, *73*, 4793–4815. <https://doi.org/10.1175/jas-d-16-0106.1>
- Chen, X., Zhao, K., Xue, M., Zhou, B., Huang, X., & Xu, W. (2015). Radar-observed diurnal cycle and propagation of convection over the Pearl River Delta during Mei-Yu season. *Journal of Geophysical Research: Atmospheres*, *120*, 2015JD023872. <https://doi.org/10.1002/2015jd023872>
- Cheng, F. Y., Hsu, Y. C., Lin, P. L., & Lin, T. H. (2013). Investigation of the Effects of Different Land Use and Land Cover Patterns on Mesoscale Meteorological Simulations in the Taiwan Area. *Journal of Applied Meteorology and Climatology*, *52*, 570–587. <https://doi.org/10.1175/jamc-d-12-0109.1>
- Collins, W. D., Rasch, P. J., Boville, B. A., Hack, J. J., Mccaa, J. R., Williamson, D. L., & Kiehl, J. T. (2004). *Description of the NCAR Community Atmosphere Model (CAM 3.0)*. NCAR Technical Note NCAR/TN-464+STR, <https://doi.org/10.5065/D63N21CH.226>
- Ding, Y. (1992). Summer Monsoon Rainfalls in China. *Journal of the Meteorological Society of Japan. Ser. II*, *70*, 373–396. https://doi.org/10.2151/jmsj1965.70.1b_373
- Dong, W. H., Lin, Y. L., Wright, J. S., Ming, Y., Xie, Y. Y., Wang, B., & Luo, Y. (2016). Summer rainfall over the southwestern Tibetan Plateau controlled by deep convection over the Indian subcontinent. *Nature Communications*, *7*. <https://doi.org/10.1038/ncomms10925>
- Du, Y., & Chen, G. X. (2018). Heavy Rainfall Associated with Double Low-Level Jets over Southern China. Part I: Ensemble-Based Analysis. *Monthly Weather Review*, *146*, 3827–3844. <https://doi.org/10.1175/mwr-d-18-0101.1>
- Du, Y., & Chen, G. X. (2019). Heavy Rainfall Associated with Double Low-Level Jets over Southern China. Part II: Convection Initiation. *Monthly Weather Review*, *147*, 543–565. <https://doi.org/10.1175/mwr-d-18-0102.1>
- Du, Y., & Rotunno, R. (2018). Diurnal Cycle of Rainfall and Winds near the South Coast of China. *Journal of the Atmospheric Sciences*, *75*, 2065–2082. <https://doi.org/10.1175/jas-d-17-0397.1>
- Furtado, K., Field, P., Luo, Y. L., Zhou, T. J., & Hill, A. (2020). The effects of cloud-aerosol interaction complexity on simulations of presummer rainfall over southern China. *Atmospheric Chemistry and Physics*, *20*, 5093–5110. <https://doi.org/10.5194/acp-20-5093-2020>
- Furtado, K., Field, P. R., Luo, Y. L., Liu, X., Guo, Z., Zhou, T. J., et al. (2018). Cloud Microphysical Factors Affecting Simulations of Deep Convection During the Presummer Rainy Season in Southern China. *Journal of Geophysical Research-Atmospheres*, *123*, 10477–10505. <https://doi.org/10.1029/2017jd028192>
- He, L., Chen, T., & Kong, Q. (2016). A Review of Studies on Prefrontal Torrential Rain in South China. *Journal of Applied Meteorological Science*, *27*, 559–569 (in Chinese).
- Hu, X. M., & Xue, M. (2016). Influence of Synoptic Sea-Breeze Fronts on the Urban Heat Island Intensity in Dallas-Fort Worth, Texas. *Monthly Weather Review*, *144*, 1487–1507. <https://doi.org/10.1175/mwr-d-15-0201.1>
- Hu, X. M., Klein, P. M., Xue, M., Lundquist, J. K., Zhang, F. Q., & Qi, Y. C. (2013). Impact of Low-Level Jets on the Nocturnal Urban Heat Island Intensity in Oklahoma City. *Journal of Applied Meteorology and Climatology*, *52*, 1779–1802. <https://doi.org/10.1175/jamc-d-12-0256.1>
- Hu, X. M., Nielsen-Gammon, J. W., & Zhang, F. Q. (2010). Evaluation of Three Planetary Boundary Layer Schemes in the WRF Model. *Journal of Applied Meteorology and Climatology*, *49*, 1831–1844. <https://doi.org/10.1175/2010jamc2432.1>
- Huang, S., Li, Z., Bao, C., Yu, Z., Chen, H., Yu, S., et al. (1986). *Heavy Rainfall over Southern China in the Pre-Summer Rainy Season*. Guangdong Science and Technology Press, 244p (in Chinese).
- Jiang, Z., Zhang, D.-L., Xia, R., & Qian, T. (2017). Diurnal Variations of Presummer Rainfall over Southern China. *Journal of Climate*, *30*, 755–773. <https://doi.org/10.1175/jcli-d-15-0666.1>
- Jin, X., Wu, T. W., & Li, L. (2013). The quasi-stationary feature of nocturnal precipitation in the Sichuan Basin and the role of the Tibetan Plateau. *Climate Dynamics*, *41*, 977–994. <https://doi.org/10.1007/s00382-012-1521-y>
- Joyce, R. J., Janowiak, J. E., Arkin, P. A., & Xie, P. P. (2004). CMORPH: A method that produces global precipitation estimates from passive microwave and infrared data at high spatial and temporal resolution. *Journal of Hydrometeorology*, *5*, 487–503. [https://doi.org/10.1175/1525-7541\(2004\)005<0487:camtpg>2.0.co;2](https://doi.org/10.1175/1525-7541(2004)005<0487:camtpg>2.0.co;2)
- Li, H. Q., Wan, Q. L., Peng, D. D., Liu, X. T., & Xiao, H. (2020a). *Multiscale analysis of a record-breaking heavy rainfall event in Guangdong, China*. *Atmospheric Research*, *232*. <https://doi.org/10.1016/j.atmosres.2019.104703>
- Li, J., Yu, R. C., & Zhou, T. J. (2008). Seasonal Variation of the Diurnal Cycle of Rainfall in Southern Contiguous China. *Journal of Climate*, *21*, 6036–6043. <https://doi.org/10.1175/2008jcli2188.1>
- Li, M. M., Song, Y., Huang, X., Li, J. F., Mao, Y., Zhu, T., et al. (2014). Improving mesoscale modeling using satellite-derived land surface parameters in the Pearl River Delta region, China. *Journal of Geophysical Research: Atmospheres*, *119*, 6325–6346. <https://doi.org/10.1002/2014jd021871>
- Li, P., Furtado, K., Zhou, T., Chen, H., & Li, J. (2021). Convection-permitting modelling improves simulated precipitation over the central and eastern Tibetan Plateau. *Quarterly Journal of the Royal Meteorological Society*, *147*, 341–362. <https://doi.org/10.1002/qj.3921>
- Li, P., Furtado, K., Zhou, T., Chen, H., Li, J., Guo, Z., & Xiao, C. (2020b). The diurnal cycle of East Asian summer monsoon precipitation simulated by the Met Office Unified Model at convection-permitting scales. *Climate Dynamics*, *55*, 131–151. <https://doi.org/10.1007/s00382-018-4368-z>

- Liu, X., Luo, Y., Huang, L., Zhang, D. L., & Guan, Z. (2020). Roles of Double Low-Level Jets in the Generation of Coexisting Inland and Coastal Heavy Rainfall Over South China During the Presummer Rainy Season. *Journal of Geophysical Research: Atmospheres*, *125*. <https://doi.org/10.1029/2020jd032890>
- Lu, H. (2019). The major research advance of rainstorm and heavy precipitation regarding the mesoscale weather dynamics in south of Yangtze-Huaihe River basin. *Torrential Rain and Disasters*, *38*, 440–449 (in Chinese).
- Luo, Y. L., Wang, H., Zhang, R. H., Qian, W. M., & Luo, Z. Z. (2013). Comparison of Rainfall Characteristics and Convective Properties of Monsoon Precipitation Systems over South China and the Yangtze and Huai River Basin. *Journal of Climate*, *26*, 110–132. <https://doi.org/10.1175/jcli-d-12-00100.1>
- Luo, Y. L., Wu, M. W., Ren, F. M., Li, J., & Wong, W. K. (2016). Synoptic Situations of Extreme Hourly Precipitation over China. *Journal of Climate*, *29*, 8703–8719. <https://doi.org/10.1175/jcli-d-16-0057.1>
- Luo, Y. L., Xia, R. D., & Chan, J. C. L. (2020). Characteristics, Physical Mechanisms, and Prediction of Pre-summer Rainfall over South China: Research Progress during 2008–2019. *Journal of the Meteorological Society of Japan*, *98*, 19–42. <https://doi.org/10.2151/jmsj.2020-002>
- Luo, Y. L., Zhang, R. H., Wan, Q. L., Wang, B., Wong, W. K., Hu, Z. Q., et al. (2017). The Southern China Monsoon Rainfall Experiment (Scmrex). *Bull. Amer. Meteor. Soc.*, *98*, 999–1013. <https://doi.org/10.1175/bams-d-15-00235.1>
- Lv, J. (1942). Nocturnal precipitation in Bashan. *Acta Meteorol Sin*, 36–53.
- Morrison, H., Curry, J. A., & Khvorostyanov, V. I. (2005). A new double-moment microphysics parameterization for application in cloud and climate models. Part I: Description. *Journal of Atmospheric Sciences*, *62*, 1665–1677. <https://doi.org/10.1175/jas3446.1>
- Pan, Y., Shen, Y., Yu, J., & Xiong, A. (2015). An experiment of high-resolution gauge-radar-satellite combined precipitation retrieval based on the Bayesian merging method. *Acta Meteorologica Sinica (in chinese)*, *73*, 177–186.
- Pleim, J. E. (2007). A Combined Local and Nonlocal Closure Model for the Atmospheric Boundary Layer. Part I: Model Description and Testing. *Journal of Applied Meteorology and Climatology*, *46*, 1383–1395. <https://doi.org/10.1175/jam2539.1>
- Pleim, J. E., & Xiu, A. (1995). Development and testing of a surface flux and planetary boundary layer model for application in mesoscale models. *Journal of Applied Meteorology*, *34*, 16–32. <https://doi.org/10.1175/1520-0450-34.1.16>
- Romatschke, U., & Houze, R. A. (2011). Characteristics of Precipitating Convective Systems in the South Asian Monsoon. *Journal of Hydrometeorology*, *12*, 3–26. <https://doi.org/10.1175/2010jhm1289.1>
- Romine, G. S., Rotunno, R., & Bluestein, H. B. (2018). A Simple Model for the Anomalous Counterclockwise Turning of the Surface Wind with Time over the Great Plains of the United States. *Journal of the Atmospheric Sciences*, *75*, 2971–2981.
- Shen, Y., Zhao, P., Pan, Y., & Yu, J. J. (2014). A high spatiotemporal gauge-satellite merged precipitation analysis over China. *Journal of Geophysical Research-Atmospheres*, *119*, 3063–3075. <https://doi.org/10.1002/2013jd020686>
- Shi, C. X., Xie, Z. H., Qian, H., Liang, M. L., & Yang, X. C. (2011). China land soil moisture EnKF data assimilation based on satellite remote sensing data. *Science China-Earth Sciences*, *54*, 1430–1440. <https://doi.org/10.1007/s11430-010-4160-3>
- Simpson, J. E. (1996). Diurnal Changes in Sea-Breeze Direction. *Journal of Applied Meteorology and Climatology*, *35*, 1166–1169. [https://doi.org/10.1175/1520-0450\(1996\)035<1166:dcisbd>2.0.co;2](https://doi.org/10.1175/1520-0450(1996)035<1166:dcisbd>2.0.co;2)
- Sun, J., & Zhang, F. (2012). Impacts of Mountain–Plains Solenoid on Diurnal Variations of Rainfalls along the Mei-Yu Front over the East China Plains. *Monthly Weather Review*, *140*, 379–397. <https://doi.org/10.1175/mwr-d-11-00041.1>
- Sun, J. H., Zhang, Y. C., Liu, R. X., Fu, S. M., & Tian, F. Y. (2019). A Review of Research on Warm-Sector Heavy Rainfall in China. *Advances in Atmospheric Sciences*, *36*, 1299–1307. <https://doi.org/10.1007/s00376-019-9021-1>
- Tao, S. (1980). *Heavy Rainfalls in China (in Chinese)*. Science Press, 225.
- van Stratum, B. J. H., Vilá-Guerau de Arellano, J., van Heerwaarden, C. C., & Ouwersloot, H. G. (2014). Subcloud-Layer Feedbacks Driven by the Mass Flux of Shallow Cumulus Convection over Land. *Journal of the Atmospheric Sciences*, *71*, 881–895. <https://doi.org/10.1175/jas-d-13-0192.1>
- Wang, H., Luo, Y. L., & Jou, B. J. D. (2014). Initiation, maintenance, and properties of convection in an extreme rainfall event during SCMREX: Observational analysis. *Journal of Geophysical Research-Atmospheres*, *119*, 13206–13232. <https://doi.org/10.1002/2014jd022339>
- Wu, M. W., Luo, Y. L., Chen, F., & Wong, W. K. (2019). Observed Link of Extreme Hourly Precipitation Changes to Urbanization over Coastal South China. *Journal of Applied Meteorology and Climatology*, *58*, 1799–1819. <https://doi.org/10.1175/jamc-d-18-0284.1>
- Wu, N. G., Zhuang, X. R., Min, J. Z., & Meng, Z. Y. (2020). Practical and Intrinsic Predictability of a Warm-Sector Torrential Rainfall Event in the South China Monsoon Region. *Journal of Geophysical Research-Atmospheres*, *125*. <https://doi.org/10.1029/2019jd031313>
- Wu, Y., Huang, A., Huang, D., Chen, F., Yang, B., Zhou, Y., et al. (2018). Diurnal variations of summer precipitation over the regions east to Tibetan Plateau. *Climate Dynamics*, *51*, 4287–4307. <https://doi.org/10.1007/s00382-017-4042-x>
- Xu, W., Zipser, E. J., & Liu, C. (2009). Rainfall Characteristics and Convective Properties of Mei-Yu Precipitation Systems over South China, Taiwan, and the South China Sea. Part I: TRMM Observations. *Monthly Weather Review*, *137*, 4261–4275. <https://doi.org/10.1175/2009mwr2982.1>
- Xue, M., Luo, X., Zhu, K. F., Sun, Z. Q., & Fei, J. F. (2018). The Controlling Role of Boundary Layer Inertial Oscillations in Meiyu Frontal Precipitation and Its Diurnal Cycles Over China. *Journal of Geophysical Research-Atmospheres*, *123*, 5090–5115. <https://doi.org/10.1029/2018jd028368>
- Yan, M., Chan, J. C. L., & Zhao, K. (2020). Impacts of Urbanization on the Precipitation Characteristics in Guangdong Province, China. *Advances in Atmospheric Sciences*, *37*, 696–706. <https://doi.org/10.1007/s00376-020-9218-3>
- Yin, J. F., Zhang, D. L., Luo, Y. L., & Ma, R. Y. (2020). On the Extreme Rainfall Event of 7 May 2017 over the Coastal City of Guangzhou. Part I: Impacts of Urbanization and Orography. *Monthly Weather Review*, *148*, 955–979. <https://doi.org/10.1175/mwr-d-19-0212.1>
- Yu, B., Zhu, K., Xue, M., & Zhou, B. (2020). Using new neighborhood-based intensity-scale verification metrics to evaluate WRF precipitation forecasts at 4 and 12 km grid spacings. *Atmospheric Research*, *246*, 105117. <https://doi.org/10.1016/j.atmosres.2020.105117>
- Zhang, M. R., & Meng, Z. Y. (2019). Warm-Sector Heavy Rainfall in Southern China and Its WRF Simulation Evaluation: A Low-Level-Jet Perspective. *Monthly Weather Review*, *147*, 4461–4480. <https://doi.org/10.1175/mwr-d-19-0110.1>
- Zhang, Q. H., Ni, X., & Zhang, F. Q. (2017). Decreasing trend in severe weather occurrence over China during the past 50 years. *Scientific Reports*, *7*. <https://doi.org/10.1038/srep42310>
- Zhang, Y. H., Xue, M., Zhu, K. F., & Zhou, B. W. (2019). What Is the Main Cause of Diurnal Variation and Nocturnal Peak of Summer Precipitation in Sichuan Basin, China? The Key Role of Boundary Layer Low-Level Jet Inertial Oscillations. *Journal of Geophysical Research-Atmospheres*, *124*, 2643–2664. <https://doi.org/10.1029/2018jd029834>
- Zhao, Y., Huang, A., Kan, M., Dong, X., Yu, X., Wu, Y., et al. (2020). Characteristics of Hourly Extreme Precipitation along the Yangtze River Basin, China during Warm Season. *Scientific Reports*, *10*, 5613. <https://doi.org/10.1038/s41598-020-62535-5>
- Zheng, Yong-guang, Chen, & Jiong (2013). A CLIMATOLOGY OF DEEP CONVECTION OVER SOUTH CHINA AND THE ADJACENT WATERS DURING SUMMER. *Journal of Tropical Meteorology*, *19*.

- Zheng, W. Z., Ek, M., Mitchell, K., Wei, H. L., & Meng, J. S. (2017). Improving the Stable Surface Layer in the NCEP Global Forecast System. *Monthly Weather Review*, *145*, 3969–3987. <https://doi.org/10.1175/mwr-d-16-0438.1>
- Zheng, Y., Xue, M., Li, B., Chen, J., & Tao, Z. (2016). Spatial characteristics of extreme rainfall over China with hourly through 24-hour accumulation periods based on national-level hourly rain gauge data. *Advances in Atmospheric Sciences*, *33*, 1218–1232. <https://doi.org/10.1007/s00376-016-6128-5>
- Zhu, K., & Xue, M. (2016). Evaluation of WRF-based convection-permitting multi-physics ensemble forecasts over China for an extreme rainfall event on 21 July 2012 in Beijing. *Advances in Atmospheric Sciences*, *33*, 1240–1258. <https://doi.org/10.1007/s00376-016-6202-z>
- Zhu, K., Xue, M., Zhou, B., Zhao, K., Sun, Z., Fu, P., et al. (2018a). Evaluation of Real-Time Convection-Permitting Precipitation Forecasts in China During the 2013–2014 Summer Season. *Journal of Geophysical Research: Atmospheres*, *123*, 1037–1064. <https://doi.org/10.1002/2017jd027445>
- Zhu, L. M., Liu, J. Z., Zhu, A. X., Sheng, M. L., & Duan, Z. (2018b). Spatial Distribution of Diurnal Rainfall Variation in Summer over China. *Journal of Hydrometeorology*, *19*, 667–678. <https://doi.org/10.1175/jhm-d-17-0176.1>